Available online at www.sciencedirect.com
ScienceDirect
Comput. Methods Appl. Mech. Engrg. xxx (xxxx) xxx
Computer methods in applied mechanics and engineering
www.elsevier.com/locate/cma

Toward selecting optimal predictive multiscale models

Jingye Tan[a], Baoshan Liang[a], Pratyush Kumar Singh[a], Kathryn A. Farrell-Maupin[b], Danial Faghihi[a,*]

[a] *Department of Mechanical and Aerospace Engineering, University at Buffalo, United States of America*
[b] *Sandia National Laboratories, United States of America*

Available online xxxx

A special issue in honor of the lifetime achievements of J. Tinsley Oden

Abstract

This work presents a systematic strategy for selecting an "optimal" predictive computational model among a set of possible mechanistic models of a physical system. To this end, the Occam-Plausibility Algorithm (Farrell-Maupin et al., 2015) is extended by introducing a method for the design of model-specific validation experiments to provide data that portray the features of the prediction quantities of interest. Leveraging Bayesian inference and model plausibility, the framework adaptively balances the trade-off between complexity and validity of the models while taking into account the uncertainty in data, model parameters, and the choice of the model itself for making reliable computational predictions. An application of this framework is demonstrated in discrete-continuum multiscale modeling of size-dependent plasticity in polycrystalline materials, involving dislocation dynamics simulations and strain gradient plasticity models.

This study suggests that the effectiveness of validation experiments relies upon the choice of the model; thus, a validation data set that adequately informs a predictive computational model may not be effective for validating other models. Additionally, the multiscale modeling results show that, given the discrete dislocation dynamics data, the optimal strain gradient plasticity model for predicting the deformation of a microelectromechanical system is obtained by excluding the isotropic hardening mechanism.

Keywords: Bayesian inference; Model selection; Uncertainty quantification; Discrete dislocation dynamics; Strain gradient plasticity

1. Introduction

The last decade has seen an explosion of observational data obtained from measurements, images, and high-fidelity simulations of complex physical systems. Concurrently, the advancements in computational science have provided remarkable opportunities to harness such a data revolution to push forward prediction capabilities of mechanistic (physics-based) models for making high-consequence decisions. An essential step in the scientific prediction of physical phenomena beyond observation is assessing the validity of models in the presence of uncertainties in data, model parameters, and numerical errors, e.g., [1–5]. However, selecting the models for predicting key Quantities of Interest (QoIs), among the many possible models depicting a physical event, poses

* Corresponding author.
E-mail address: danialfa@buffalo.edu (D. Faghihi).

https://doi.org/10.1016/j.cma.2022.115517
0045-7825/

Nomenclature

Uncertainty Quantification

$\boldsymbol{\theta}$	Vector of model parameters
Θ	Parameter space
$\mathbb{E}$	Mean
$\mathbb{V}$	Variance
$\mathbf{D}$	Observational data
$\mathbf{D}_c$	Calibration data
$\mathbf{D}_v$	Validation data
$\mathcal{D}$	Data space
$\mathbf{I}$	Identity matrix
$\mathcal{M}$	Set of parametric models
$\mathcal{N}$	Gaussian distribution
$\mathcal{S}$	Scenario
$\mathcal{S}_c$	Calibration scenario
$\mathcal{S}_v$	Validation scenario
$\mathcal{S}_p$	Prediction scenario
$\mathcal{U}$	Uniform distribution
π	Probability density function
π_{post}	Posterior probability density function
π_{prior}	Prior probability density function
π_{like}	Likelihood probability density function
π_{evid}	Evidence probability density function
ρ	Model Plausibility
σ^2_{noise}	Noise variance
$\boldsymbol{\epsilon}$	Total error
$\boldsymbol{\mathcal{Y}}, \mathcal{Y}$	Multivariate/univariate model output
D_{KL}	Kullback–Leibler divergence
M	A parametric computational model
S	Total effect sensitivity index
m	Noise multiplier

Discrete Dislocation Dynamics

$\mathbf{r}$	Position of a point on the dislocation
$\delta\mathbf{r}$	Position change of a point on the dislocation
$\mathbf{B}_\alpha$	Diagonal resistive matrix of a dislocation α
$\mathbf{b}_j$	Burgers vector of dislocation segment j
$\mathbf{E}$	Strain tensor
$\mathbf{F}$	Total force acting on a dislocation
$\mathbf{n}^\beta$	Normal of slip plane β
$\mathbf{p}$	Dislocation line vector
F_k	Global force vector
$\mathbf{T}$	Stress tensor
$\mathbf{v}_\alpha$	Velocity of the dislocation α
$\mathbf{v}_j^\beta$	Velocity of the segment j and plane β
$\mathcal{C}$	Fourth order elastic tensor

μ	Shear modulus
ν	Poisson's Ratio
B_{ki}	Global resistivity matrix
C	Dislocation path
D	Grain size
H	Film thickness
l_j^β	Length of dislocation segment j moving on the slip plane β
Q_i	Global coordinates of degrees of freedom of segments
V	Volume of the simulated crystal

Strain Gradient Plasticity

$\boldsymbol{\Psi}$	Specific free energy per unit volume
∇	Gradient operator
Δ	Laplacian operator
Δt_n	n^{th} time interval
$\dot{P}$	Effective non-local flow rate
ℓ_{dis}	Dissipative length scale
ℓ_{en}	Energetic length scale
ϵ_{ijk}	Permutation tensor
η	Regularization parameter
Γ_D, Γ_N	Macroscopic boundaries of the domain
Γ_F, Γ_H	Microscopic boundaries of the domain and grain boundaries
λ, μ	Lamé constants
$\mathbb{S}$	Third-order microstress tensor conjugate to the gradient of plastic strain tensor
$\mathbb{S}_{\text{dis}}$, $\mathbb{S}_{\text{en}}$	Energetic/dissipative components of $\mathbb{S}$
$\mathbf{S}$	Second-order equivalent microstress tensor conjugate to the gradient of plastic strain
$\mathbf{Q}$	Second-order microstress tensor conjugate to the plastic strain
$\mathbf{Q}_{\text{dis}}$, $\mathbf{Q}_{\text{en}}$	Energetic/dissipative components of $\mathbf{Q}$
Q	First-order microstress tensor conjugate to the equivalent plastic strain
$\mathbf{E}^e$	Elastic strain tensor
$\mathbf{E}^p$	Plastic strain tensor
$\mathbf{E}^{p\dagger}$	Prescribed plastic strain tensor
$\mathbf{f}$	Body force
$\mathbf{G}$	Burgers tensor
$\mathbf{N}^p$	Direction of plastic flow
$\mathbf{n}_N$	Outward unit normal to the Neumann boundary
$\mathbf{n}_F$	Outward unit normal to the grain boundaries
$\mathbf{T}$	Cauchy stress tensor
$\mathbf{T}_0$	Deviatoric part of Cauchy stress tensor
$\mathbf{t}$	Surface traction vector
$\mathbf{u}$	Displacement vector
$\mathbf{u}^\dagger$	Prescribed displacement vector
$\mathbf{x}$	Position of a material point
x, y, z	Orthonormal Cartesian coordinates
Ω	Bounded Lipschitz domain
E	Young's modulus
h, r	Isotropic hardening parameters

p	Equivalent plastic strain
t	Time
$\mathcal{V}$	Vector Hilbert space
$\boldsymbol{v}$	Vector test function
$\mathcal{W}$	Scalar Hilbert space
w	Scalar test function
Y	Yield stress
Miscellaneous	
e	Uniaxial tensile strain
e_f	Applied tensile strain
T	Uniaxial tensile stress

a major challenge in predictive computational modeling. For example, the building blocks in developing physically meaningful continuum mechanics models are the fundamental balance of laws of mass, linear and angular momentum, and energy, which are supplemented by postulating constitutive equations based on physical and thermodynamical constraints, e.g., [6,7]. While the former components are reliable, the constitutive equations often incur model inadequacy due to simplifying assumptions on physical realities. Additionally, there can be many possible choices of constitutive relations for a class of bodies undergoing specific processes, leading to a set of continuum models with different fidelities, complexities, and computational costs. For other examples of possible model classes, the reader is referred to [8,9] for molecular dynamics simulations and [10] for agent-based models of cancer cells evolution. Therefore, reliable computational prediction requires a systematic approach to balancing the trade-off between model complexity and validity for selecting the "optimal" model for prediction.

The Occam Plausibility Algorithm (OPAL), introduced in Farrell et al. [8], offers an adaptive framework to model validation and selection. The name is derived from the principle of Occam's Razor, which states that among competing theories, the one that relies on the fewest assumptions is the best. Following this principle, OPAL leverages output sensitivities to parameter variances, model validation, and the notation of model plausibility to determine the *simplest valid model* from a collection of possible mechanistic models of a physical process, given a set of observational data. The algorithm relies on Bayesian inference to quantify uncertainties in data and model and presents an adaptive bottom-up strategy by the successive increase in model complexity until the validation criteria are fulfilled. OPAL has been successfully implemented to select and validate coarse-grained models of atomistic systems of polymeric materials [8] and continuum models of tumor growth and radiotherapy using medical imaging data [11–13].

Although progress has been made in recent years in methods and algorithms supporting predictive physics-based modeling, many open problems remain to be addressed. A fundamental aspect of model validation is that a model may be valid for predicting one particular QoI but invalid for another [1]. Generally, the target prediction is the quantities not accessible by observational data. Thus the physics-based model must extrapolate the data obtained in the validation experiments to predict the QoI beyond the data range. The overriding importance of the validation data in predictive modeling gives rise to a grand challenge in designing model validation tests that produce observational data representing the target prediction.

This contribution provides a systematic strategy for selecting "optimal predictive models" among the numerous possible models that deliver a sufficiently accurate computational prediction. We extend OPAL by introducing the notation of *model-specific validation experiments* by the realization that a set of validation data that adequately informs the model parameters essential for the target prediction may not be effective for other models. Based on global sensitivity analyses of the model parameters in the validation and prediction scenarios, we propose a method to design validation experiments to provide observational data reflecting, in some sense, the structure of the prediction QoI. Consequently, the modified algorithm adaptively selects the "optimal model", which refers to balancing the trade-off between the model complexity and validity while leveraging the model-specific data for validation that warrants the "predictive" capacity of the model.

The modeling problem considered herein is a class of discrete-to-continuum multiscale models of plastic deformation in polycrystalline materials. The high-fidelity model is the discrete dislocation dynamics simulation that explicitly simulates the microstructural evolutions leading to plastic deformation, e.g., [14]. The multiscale approach consists of the hierarchical transition from the discrete simulations to strain gradient plasticity continuum models that leverage length parameters to characterize size-dependent plastic responses of microscale materials, e.g., [15,16]. The target prediction in this work is the response of a microelectromechanical (MEMS) pressure sensor under plastic deformation in which the observational data from the discrete dislocation simulations is inaccessible. The main challenge in this class of multiscale modeling is the choice of strain gradient plasticity model that can deliver acceptable computational prediction, given the uncertain data furnished by the discrete stochastic model. To address this challenge, different strain gradient plasticity models are constructed by combinations of various micromechanical mechanisms governing the plastic responses of small-scale materials. The modified OPAL is then implemented to select an optimal continuum model for predicting the QoI using the data furnished by the discrete dislocation simulations on the materials subsystems while coping with uncertainty in data due to microstructure randomness and modeling errors incurred by simplifying assumptions in the theoretical model and numerical solutions.

Following this introduction, we present an overview of discrete dislocation and continuum strain gradient models of microscale plasticity of materials systems. Uncertainty quantification methods of the physics-based models and the modified version of the Occam-Plausibility Algorithm are detailed in Section 3. Section 4 provides an example of selecting the optimal predictive model with application to the sequential multiscale modeling of polycrystalline materials systems. Finally, concluding remarks can be found in Section 5.

2. Multiscale model of microscale plasticity

The multiscale modeling of size-dependent plasticity in polycrystalline materials in this work consists of up-scaling discrete dislocation dynamics (high-fidelity) simulations to continuum strain-gradient plasticity (low-fidelity) models. This section summarizes the basics of each model.

2.1. Discrete dislocation dynamics simulations

In a class of three-dimensional (3D) discrete dislocation dynamics (DDD) simulations, e.g., [17–20], the individual dislocations are represented as spatial curves connected through dislocation nodes, and third-order shape functions maintain continuity of dislocation lines at the nodes. The 3D dislocation motion is described by kinetic equations for the time evolution of generalized coordinates, consisting of position and tangent vectors at segment nodes. The equation of motion of the α-th dislocation is based on a variational principle for Gibbs free energy and derived from irreversible thermodynamics as [17],

$$\int_C (\mathbf{F} - \mathbf{B}_\alpha \mathbf{v}_\alpha)\delta\mathbf{r}|d\mathbf{p}| = 0, \tag{1}$$

where $\mathbf{F}$ is the total force acting on a dislocation from the summation of the Peach–Koehler, self-force, and Osmotic forces [19], $\mathbf{v}_\alpha$ is the velocity of the dislocation, $\mathbf{B}_\alpha$ is the diagonal resistive matrix (inverse of dislocation mobility), $\mathbf{p}$ is the dislocation line vector over the path C, $\mathbf{r}$ is the position of a point on the dislocation, and $\delta\mathbf{r}$ describes the change in position for atoms on the dislocation line. Dividing the dislocation line into segments, the equation of motion (1) can be written as [19],

$$F_k = \sum_{i=1}^{N_{seg}} B_{ki} \frac{\partial}{\partial t}(Q_i), \tag{2}$$

where Q_i are global coordinates of degrees of freedom of segments, i.e., the position and tangent at a specific node, B_{ki} is the global resistivity matrix, F_k is the global force vector, and N_{seg} is the total number of degrees of freedom, i.e., number of coordinates at two ends of the loop segment multiplied by the number of segments. The coordinates are updated by solving (2), and the macroscopic plastic strain rate is calculated from the motion of dislocations in microscale using [18],

$$\dot{\mathbf{E}}^p = \frac{1}{2V} \sum_{j=1}^{N_s} l_j^\beta \mathbf{v}_j^\beta (\mathbf{b}_j \otimes \mathbf{n}^\beta + \mathbf{n}^\beta \otimes \mathbf{b}_j), \tag{3}$$

where V is the volume of the simulated crystal, N_s is the total number of dislocation segments, l_j^β is the length of dislocation segment j moving on the slip plane β, $\mathbf{v}_j^\beta$ is the corresponding velocity of the segment j, $\mathbf{b}_j$ and $\mathbf{n}^\beta$ are the Burgers vector of dislocation segment j and the normal of slip plane β, respectively. The stress $\mathbf{T}$ and strain $\mathbf{E}$ relation is expressed as,

$$\dot{\mathbf{T}} = \mathcal{C}(\dot{\mathbf{E}} - \dot{\mathbf{E}}^p), \tag{4}$$

where $\mathcal{C}$ is the elastic tensor including shear modulus μ and Poisson's ratio ν parameters. Eq. (4) is solved incrementally under a constant strain rate assumption. More details on this class of DDD model can be found in [17–19].

This work leverages the DDD simulations of size-dependent plasticity in polycrystalline Copper thin films conducted by Zhou and LeSar [20]. The domain consists of nine columnar grains with the grain size D and film thickness H (see the schematics in Fig. 4). The stochastic mechanism of thermally-activated cross-slip is modeled using the Monte Carlo approach to determine the activation of cross-slip. Furthermore, the dislocation transmission across grain boundaries is taken into account using a line-tension model that allows for dislocation transfer once the resolved shear stress of a dislocation exceeds the grain boundary transmission strength. The thin films are subjected to uniaxial tensile loading with a constant strain rate of 2000 s^{-1}. To characterize the microstructural randomness on the size-dependent plasticity responses, the DDD simulations are conducted for different initial distributions of Frank–Read sources with random lengths with the initial dislocation densities of approximately 1.0×10^{13} m^{-2}. In all simulations, the DDD model parameters are considered as μ= 50 GPa, ν= 0.34, dislocation mobility is $10^{-4}Pa^{-1}s^{-1}$, and the ratio of the grain boundary transmission strength to the critical stress for activating the Frank–Read source is 5. For developing the multiscale model, we use the DDD stress–strain results at the center grain for different film thicknesses H and grain sizes D. Fig. 1 shows the extracted data points (from Figure 8 of Zhou and LeSar [20], p.193) leveraged to inform the continuum model. The computed stress–strain data from the DDD simulations in this figure clearly show the plastic deformation's dependency on the domain's size. The error bars in Fig. 1 indicate the averaged stress over ten separate simulations with different initial dislocation configurations.

2.2. Continuum strain gradient plasticity theory

The strain-gradient plasticity theory of Faghihi and Voyiadjis [16,21–23] is taken into account as the continuum model in this work. The original version of this theory is built on earlier works of Gurtin and co-workers, e.g., [24–26] and accounts for fully thermo-mechanical plastic deformation in microscale materials under fast transient heating. A summary of the governing equations of a simplified model used in this work, after ignoring the generalized heat equation and the grain boundary effect, is provided in this section.

Let Ω be a bounded Lipschitz domain in three-dimensional space, $\mathbf{x}$ be the position of a material point, and $\mathbf{u}(\mathbf{x}, t)$ is the displacement of the body from its reference configuration. Under small deformation assumption, the strain is decomposed according to,

$$\mathbf{E} = \mathrm{sym}(\nabla\mathbf{u}) = \mathbf{E}^e + \mathbf{E}^p, \tag{5}$$

where $\mathbf{E}^e$ and $\mathbf{E}^p$ denote the elastic and plastic strains and plastic incompressibility $\mathrm{tr}(\mathbf{E}^p) = 0$ and plastic irrotationality $\mathrm{skw}(\mathbf{E}^p) = \mathbf{0}$ are taken into account. The Burgers tensor [27] represents the strain-gradient effects due to the presence of geometrically necessary dislocations (GNDs) and is defined as,

$$\mathbf{G} = \nabla \times \mathbf{E}^p. \tag{6}$$

The time-derivative of the Burgers tensor is given by,

$$\dot{\mathbf{G}} = (\nabla \dot{p} \times)\mathbf{N}^p + \dot{p}(\nabla \times \mathbf{N}^p), \tag{7}$$

where $p = \|\mathbf{E}^p\|$ denotes equivalent plastic strain, $\mathbf{N}^p = \dot{\mathbf{E}}^p/\|\dot{\mathbf{E}}^p\|$ is the direction of plastic flow, and $(\nabla \dot{p} \times) = \varepsilon_{irs}\dot{p}_{,r}$ is a skew-symmetric tensor with ε_{ijk} being the permutation symbol.

Following the above kinematics, the principle of virtual power leads to the macro-force balance,

$$\nabla \cdot \mathbf{T} + \mathbf{f} = \mathbf{0}, \quad \text{in} \quad \Omega, \tag{8}$$

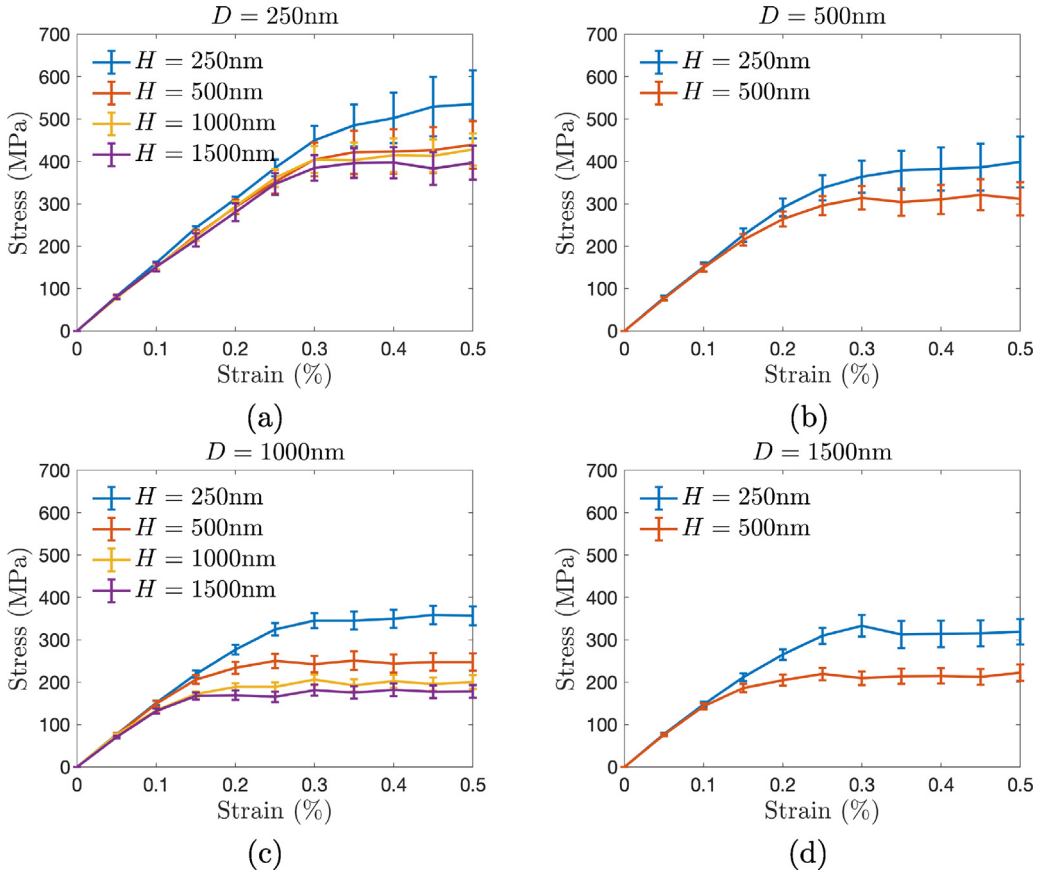

Fig. 1. Stress–strain results obtained from 3D stochastic DDD simulations of polycrystalline thin films under uniaxial tension with different film thicknesses H and grain sizes D of (a) 250 nm, (b) 500 nm, (c) 1000 nm, and (d) 1500 nm. The error bars indicate uncertainty cured by the ten separate simulations with different initial dislocation configurations.
Source: Reproduced from [20] with permission from Elsevier.

and the microforce balance,

$$\mathbf{T}_0 - \mathbf{Q} + \nabla \cdot \mathbb{S} = \mathbf{0}, \quad \text{in} \quad \Omega, \tag{9}$$

together with macroscopic and microscopic boundary conditions,

$$\mathbf{T}\mathbf{n}_N = \mathbf{t} \quad \text{on} \quad \Gamma_N, \qquad \mathbf{u} = \mathbf{u}^\dagger \quad \text{on} \quad \Gamma_D, \tag{10}$$

$$\mathbb{S}\mathbf{n}_F = \mathbf{M} \quad \text{on} \quad \Gamma_F, \qquad \mathbf{E}^p = \mathbf{E}^{p\dagger} \quad \text{on} \quad \Gamma_H. \tag{11}$$

In the above relations, $\mathbf{T}$ is the Cauchy stress tensor with the deviatoric part $\mathbf{T}_0$, $\mathbf{f}$ is the body force, $\mathbf{t}$ is the surface traction, and the second-order tensor $\mathbf{Q}$ and the third-order tensor $\mathbb{S}$ are the microforces power-conjugate to the plastic strain and its gradient, respectively. Furthermore, $\mathbf{u}^\dagger$ denotes a prescribed displacement, Γ_D and Γ_N are complementary parts of the boundary of the domain Ω, and $\mathbf{n}_N$ is the outward unit normal on the corresponding boundary. The prescribed plastic strain is denoted by $\mathbf{E}^{p\dagger}$, $\mathbf{M}$ is called the micro-traction, and Γ_H and Γ_F are either external boundaries of the domain or the internal interfaces (grain boundaries) with corresponding unit normal $\mathbf{n}_F$. We assumed the displacement field is continuous across the grain boundary, and dislocations cannot penetrate the grain boundaries. Refer to [16] for a model of grain-boundary that accounts for the energy storage due to the dislocation pile-up and energy dissipation once the dislocations transfer through the grain boundary as a result of both resistance force and change in the interfacial area.

The local dissipation inequality under isothermal conditions is expressed as [15,28],

$$\mathbf{T} : \dot{\mathbf{E}}^e + \mathbf{Q} : \dot{\mathbf{E}}^p + \mathbb{S} \vdots \nabla\dot{\mathbf{E}}^p - \dot{\Psi} \geq 0, \tag{12}$$

where Ψ is the specific Helmholtz free energy per unit volume, with the following constitutive relation

$$\Psi = \frac{1}{2}\mathbf{E}^e : \mathcal{C}\mathbf{E}^e + h\left(\|\mathbf{E}^p\| + \frac{1}{r}\exp(-r\|\mathbf{E}^p\|) - \frac{1}{r}\right) + \frac{1}{2}\mu\ell_{\text{en}}^2\|\nabla\mathbf{E}^p\|^2. \tag{13}$$

The first term on the right-hand side of (13) is the elastic component of the free energy where $\mathcal{C}$ is the fourth-order elastic tensor including the Lamé constants, μ and λ (or equivalently, Young's modulus E and Poisson's ratio ν). The second term of the free energy accounts for the interaction among slip systems, i.e., the forest dislocations, characterized by $\|\mathbf{E}^p\|$ in macroscale and leading to isotropic hardening with two model parameters h and r. We note that while isotropic hardening is a dissipative phenomenon, it can equivalently be characterized energetically [23,29]. The third term in (13) addresses the short-range interactions between GNDs moving on close slip planes, represented by plastic strain gradient and leading to kinematic hardening [24,30]. The energetic length scale parameter ℓ_{en} in this relation controls the non-local short-range interaction among GNDs [31,32]. From (13), the energetic counterparts of the thermodynamical stresses are given by,

$$\begin{aligned}
\mathbf{T} &= \frac{\partial\Psi}{\partial\mathbf{E}^e} = \lambda(\text{tr}\,\mathbf{E}^e)\mathbf{I} + 2\mu\mathbf{E}^e,\\
\mathbf{Q}_{\text{en}} &= \frac{\partial\Psi}{\partial\mathbf{E}^p} = h\,(1-\exp(-rp))\,\frac{\mathbf{E}^p}{\|\mathbf{E}^p\|},\\
\mathbb{S}_{\text{en}} &= \frac{\partial\Psi}{\partial\nabla\mathbf{E}^p} = \mu\ell_{\text{en}}^2\nabla\mathbf{E}^p.
\end{aligned} \tag{14}$$

Following the decomposition of the micro-stress additively into energetic and dissipative counterparts,

$$\mathbf{Q} = \mathbf{Q}_{\text{en}} + \mathbf{Q}_{\text{dis}}, \quad \mathbb{S} = \mathbb{S}_{\text{en}} + \mathbb{S}_{\text{dis}}, \tag{15}$$

the reduced dissipation inequality from (12) becomes [33,34]

$$\Phi = \mathbf{Q}_{\text{dis}} : \dot{\mathbf{E}}^p + \mathbb{S}_{\text{dis}} \vdots \nabla\dot{\mathbf{E}}^p \geq 0, \tag{16}$$

where Φ is the energy dissipation potential. The constitutive equations for the dissipative thermodynamical stresses for the rate-independent plastic deformation are (see [32] for details),

$$\begin{aligned}
\mathbf{Q}_{\text{dis}} &= \frac{\partial\Phi}{\partial\dot{\mathbf{E}}^p} = Y\frac{\dot{\mathbf{E}}^p}{\dot{P}},\\
\mathbb{S}_{\text{dis}} &= \frac{\partial\Phi}{\partial\nabla\dot{\mathbf{E}}^p} = Y\ell_{\text{dis}}^2\frac{\nabla\dot{\mathbf{E}}^p}{\dot{P}},
\end{aligned} \tag{17}$$

where Y is the yield stress, ℓ_{dis} is the dissipative length parameter controlling the gradient strengthening, and the effective non-local flow rate $\dot{P}$ is defined as,

$$\dot{P} = \sqrt{\|\dot{\mathbf{E}}^p\|^2 + \ell_{\text{dis}}^2\|\nabla\dot{\mathbf{E}}^p\|^2}, \tag{18}$$

that describes the energy dissipation due to the motion of both SSDs and GNDs [24,35].

Substituting the thermodynamical stresses (14) and (17), the micro-force balance (9), is written as a second-order partial-differential equation for the plastic strain,

$$\mathbf{T}_0 - \left[-\mu\ell_{\text{en}}^2\Delta\mathbf{E}^p\right] = h(1-\exp(-rp))\frac{\mathbf{E}^p}{\|\mathbf{E}^p\|} + Y\frac{\dot{\mathbf{E}}^p}{\dot{P}} - Y\ell_{\text{dis}}^2\nabla\cdot\left[\frac{\nabla\dot{\mathbf{E}}^p}{\dot{P}}\right], \tag{19}$$

where Δ is the Laplacian operator. The differential Eqs. (8) and (19), along with the constitutive relation $(14)_1$ constitute the governing equations of the strain gradient plasticity theory.

2.2.1. Classes of strain gradient models

The strain gradient plasticity theory described in the previous section accounts for various micromechanical mechanisms that arise from the thermodynamical stresses to govern the size-dependent plastic responses of

Table 1
Different model classes derived from the full strain-gradient plasticity, (19) and (8), by various combinations of the energetic and dissipative micro-stresses and examples of the analogous gradient theories in the literature.

Models	Plasticity mechanisms				Examples of equivalent plasticity theories
	$\mathbf{Q}_{\text{en}}$	$\mathbf{Q}_{\text{dis}}$	$\mathbb{S}_{\text{en}}$	$\mathbb{S}_{\text{dis}}$	
M_1		✓	✓		Aifantis [38,39]
M_2		✓		✓	Fleck and Willis [36], Niordson and Tvergaard [40], Fleck and Hutchinson [41]
M_3	✓	✓			Classical plasticity with nonlinear hardening
M_4		✓	✓	✓	Gurtin and Anand [24,42]
M_5	✓	✓	✓		Voyiadjis et al. [43–46]
M_6	✓	✓		✓	Fleck and Willis [47], Bardella [48], Fredriksson and Gudmundson [49]
M_7	✓	✓	✓	✓	Voyiadjis et al. [50,51], Bardella and Niordson [52]

small-scale materials. These mechanisms include elastic deformation ($\mathbf{T}$), forest dislocations leading to isotropic hardening ($\mathbf{Q}_{\text{en}}$), short-range interactions between GNDs leading to kinematic hardening ($\mathbb{S}_{\text{en}}$), movement of mobile dislocations resulting in plastic flow ($\mathbf{Q}_{\text{dis}}$), and GNDs induced strengthening $\mathbb{S}_{\text{dis}}$. It is possible, however, to construct a set of plasticity models with different fidelities and complexity by eliminating some of these stresses. Table 1 summarizes different model classes that can be derived by considering different combinations of stresses (micromechanical mechanisms). The models presented in this table are analogous to other gradient theories proposed in the literature regarding the contributions of various dislocation phenomena. For example, the model M_2 only accounts for the dissipative nature of dislocations, leading to gradient strengthening in plastic flow. Similarly, in the theory of Fleck and Willis [36], stress measures conjugate to plastic strain and its gradient are assumed to be dissipative in nature, and attention is paid to ensure that positive plastic work is done. For a comprehensive review of different strain gradient plasticity models and their scopes of applications, the interested readers are referred to [37] and the references cited therein.

2.2.2. Finite element solution

The computational plasticity model is developed by simplifying the theory presented in the previous section, (8) and (19), to a strain-gradient theory represented based on the scalar plasticity variable. To this end, we approximate (7) by truncating the second term $\dot{\mathbf{G}} \approx (\nabla \dot{p} \times)\mathbf{N}^p$ and assume that the co-directionality hypothesis [53] holds, which asserts that the directions of plastic flow and deviatoric stress coincide $\mathbf{N}^p \approx \mathbf{T}_0/\|\mathbf{T}_0\|$. Following these assumptions, the strong form of the governing equations consisting of macro-force and micro-force balances become

$$\begin{aligned} &\nabla \cdot \mathbf{T} = \mathbf{0}, \\ &\mathbf{T}_0 = (Q + \nabla \cdot \mathbf{S})\mathbf{N}^p, \end{aligned} \tag{20}$$

where $Q = Q_{\text{en}} + Q_{\text{dis}}$ and $\mathbf{S} = \mathbf{S}_{\text{en}} + \mathbf{S}_{\text{dis}}$ and

$$\begin{aligned} Q_{\text{en}} &= h - h\exp(-rp)\ , \quad Q_{\text{dis}} = Y\left(\frac{\dot{p}}{\dot{P}}\right), \\ \mathbf{S}_{\text{en}} &= \mu\ell_{\text{en}}^2\nabla p\ , \quad \mathbf{S}_{\text{dis}} = Y\ell_{\text{dis}}^2\left(\frac{\nabla\dot{p}}{\dot{P}}\right). \end{aligned} \tag{21}$$

Additionally, to facilitate numerical solutions, we substitute (18) with a regularized effective non-local flow rate, which is smooth everywhere except at the origin,

$$\dot{P} = \sqrt{\|\dot{p}\|^2 + \ell_{\text{dis}}^2(\nabla\dot{p}\cdot\nabla\dot{p}) + \eta^2}, \tag{22}$$

where $\eta > 0$ is a small value.

To solve the coupled nonlinear system of equations in (20), we make use of continuous Galerkin finite element methods and a dual-mixed variational formulation, involving both displacement field $\mathbf{u}$ and the equivalent plastic strain field p as separate unknowns. The Hilbert spaces are defined as,

$$\mathcal{V} = \{\boldsymbol{v} \in H^1(\Omega) : \boldsymbol{v} = \mathbf{0} \ \text{ on } \ \Gamma_D\},$$
$$\mathcal{W} = \{w \in H^1(\Omega) : w = 0 \ \text{ on } \ \Gamma_H\},$$

for the displacement and equivalent plastic strain, respectively. The variational problem, for Dirichlet boundary conditions, is then defined as: Find $(\mathbf{u}, p) \in \mathcal{V} \times \mathcal{W}$, such that

$$\left.\begin{aligned} \int_\Omega (\mathbf{T} : \nabla \boldsymbol{v})\, d\mathbf{x} &= 0 \\ \int_\Omega ((Q - \|\mathbf{T}_0\|)\, w + \mathbf{S} \cdot \nabla w)\, d\mathbf{x} &= 0 \end{aligned}\right\}, \tag{23}$$

for all choices of test functions $\boldsymbol{v} \in \mathcal{V}$ and $w \in \mathcal{W}$. For compatible spatial discretization, we approximate the displacement field $\mathbf{u}$ by the second-order Lagrange polynomial while the equivalent plastic strain p is approximated by the first-order Lagrange polynomial [15]. Such a discretization alleviates the instability and stress oscillations that can form in the solution of this class of coupled partial differential equations. The time discretization is achieved by partitioning the time interval by the increment $\Delta t_n = t_{n+1} - t_n$. The incremental problem is then obtained using a backward Euler approximation in time to solve (23) for the displacement $\mathbf{u}_{n+1}$ and equivalent plastic strain p_{n+1} from the known $(\mathbf{u}_n, p_n)$ from the previous step. The plastic strain tensor is then evaluated at each time step, using $\mathbf{E}^p_{n+1} = \mathbf{E}^p_n + \Delta t_n (p_{n+1} - p_n)\mathbf{N}^p_n$.

Extensive numerical analyses of this class of strain gradient plasticity models and the proof of existence and uniqueness of solutions are presented in [54–56]. In particular, Reddy et al. [54] showed that the numerical solution requires hardening (presence of $\mathbf{Q}_{\text{en}}$ and/or $\mathbb{S}_{\text{en}}$) to guarantee uniqueness in the local stress response. Following these studies, we leverage a generalized Newton method for solving the incremental nonlinear problem that arises from (23). The number of required Newton steps increases for smaller length scales, and the convergence rate is mesh-dependent. To reduce the prohibitive computational costs of the subsequent uncertainty analyses, we implemented an adaptive time-stepping approach in which the choice of the next time increment depends on the number of Newton steps required for the preceding time increment. Fig. 2 shows a set of 2D numerical experiments of the model on the size effect responses of a polycrystalline thin film corresponding to the domain and boundary conditions of the DDD simulations (Section 2.1). The finite element library FEniCS [57] is employed to implement the solution algorithm of the strain gradient plasticity models.

3. A framework for model validation and selection

The proposed strategy for selecting an "optimal" predictive computational model relies on the systematic assessment of uncertainty in data, model parameters, and the model itself. This section overviews the uncertainty quantification methods, including sensitivity analysis and the Bayesian approaches to parameter inference and model selection. Leveraging these methods, we then lay down the framework for adaptive selection and validation of computational models.

3.1. Forward and inverse uncertainty assessment methods

Let $\mathcal{M}$ be a set of m parametric and physics-based (mechanistic) models,

$$\mathcal{M} = \left\{M_1(\boldsymbol{\theta}_1), M_2(\boldsymbol{\theta}_2), \ldots, M_P(\boldsymbol{\theta}_P)\right\}, \tag{24}$$

where each model M_i, $i = 1, 2, \ldots, P$ has its own set of parameters $\boldsymbol{\theta}_i \in \Theta_i$. The models in the set may be related and share the same parameters. Additionally, we denote observational data by $\mathbf{D} \in \mathcal{D}$. In the context of the sequential multiscale modeling in this work, M_i denotes different strain gradient plasticity models in Table 1 and the data $\mathbf{D}$ is furnished by the DDD simulations shown in Fig. 1.

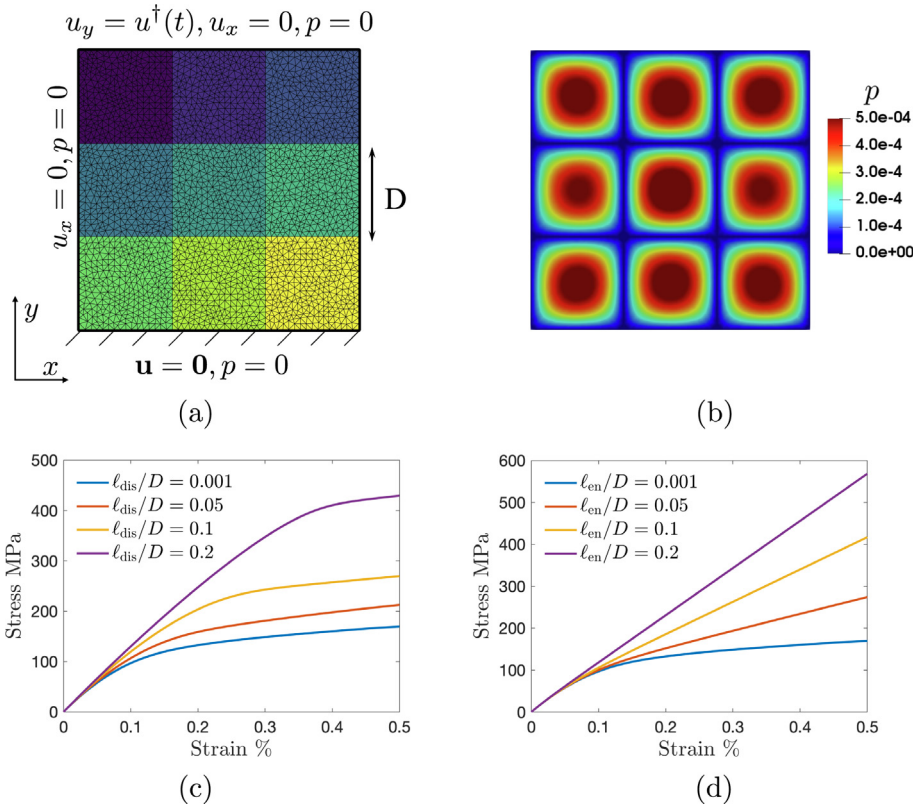

Fig. 2. Numerical experiments of the 2D polycrystalline thin film under uniaxial tensile loading using the strain gradient plasticity model: (a) Geometry and finite element mesh for the domain with the grain size of $D = 100$ nm and consists of 4914 elements. The external surfaces and grain boundaries are assumed to be impenetrable to dislocation by imposing $p = 0$; (b) Contours of equivalent plastic strain p using the $\ell_{en} = 60$ nm and $\ell_{dis} = 60$ nm; (c) Size-dependent stress–strain results due to variation of length parameter ℓ_{dis} with $\ell_{en} \approx 0$ showing that the dissipative length scale gives rise to the flow stress strengthening. (d) Size-dependent stress–strain results due to variation of length parameter ℓ_{en} with $\ell_{dis} \approx 0$ showing increasing energetic length scale leads to more significant kinematic hardening. The other parameters of the model are: $E = 125$ GPa, $Y = 100$ MPa $h = 1$ MPa, and $r = 1$.

3.1.1. Global sensitivity analysis

Global sensitivity analysis ranks the importance of model parameters in contributing to the uncertainty of the model's outputs [58–61]. We employ variance-based sensitivity analysis [62–64], in which the parameter sensitivity is calculated by the conditional variance in the model output caused by each parameter. Let $\mathcal{Y}_{M_i,\mathcal{S}}$ be a univariate output of the model M_i with K_i uncertain parameters $\boldsymbol{\theta}_i$ and for the scenario $\mathcal{S}$ in which the model is posed. The scenario refers to the features of the problem that can be specified, such as the domain and specific boundary conditions. Thus the same model can be used in several different scenarios. A variance based sensitivity measure for each parameter is the *total effect index* S defined as (see [65,66] for more details),

$$S_{k|M_i,\mathcal{S}} = 1 - \frac{\mathbb{V}_{\boldsymbol{\theta}_i^{\sim k}}\left(\mathbb{E}_{\theta_i^k}(\mathcal{Y}_{M_i,\mathcal{S}}|\boldsymbol{\theta}_i^{\sim k})\right)}{\mathbb{V}(\mathcal{Y}_{M_i,\mathcal{S}})}, \quad k = 1,\ldots,K_i, \quad i = 1,\ldots,P. \tag{25}$$

where θ_i^k is the kth input factor, $\boldsymbol{\theta}_i^{\sim k}$ is the vector of all parameters except θ_i^k, and $\mathbb{E}_{\theta_i^k}(\cdot)$ is the mean and $\mathbb{V}_i^{\boldsymbol{\theta}_{\sim k}}(\cdot)$ is the variance taken over all possible values of $\boldsymbol{\theta}_{\sim k}$ while θ_k is fixed. A small total effect index $S_{k|M_i}$ for a parameter indicates that fixing that parameter at any value within its uncertainty range will not appreciably impact the model output. Given the probability distributions of the uncertain parameters, one can leverage a Monte Carlo (MC) estimator proposed by Saltelli [59,60,65,67] to compute the total sensitivity index (25). This estimator decreases the cost of approximating multi-dimensional integrals for each model from N_{MC}^2 to $N_{MC}(K+2)$ model evaluation [59], where N_{MC} is the number of MC samples.

3.1.2. Bayesian inference

For determining the model parameters from data, we employ Bayesian inference. Bayes' Theorem [68], acknowledging that we have additional conditional information that the model $M_i(\boldsymbol{\theta}_i)$, set $\mathcal{M}$, and scenario $\mathcal{S}$ are known, is written as

$$\pi_{post}(\boldsymbol{\theta}_i|\mathbf{D}, M_i, \mathcal{M}, \mathcal{S}) = \frac{\pi_{like}(\mathbf{D}|\boldsymbol{\theta}_i, M_i, \mathcal{M}, \mathcal{S})\pi_{prior}(\boldsymbol{\theta}_i|M_i, \mathcal{M})}{\pi_{evid}(\mathbf{D}|M_i, \mathcal{M}, \mathcal{S})}, \quad i = 1, 2, \ldots, P \tag{26}$$

where $\pi_{post}(\boldsymbol{\theta}_i|\mathbf{D}, M_i, \mathcal{M}, \mathcal{S})$ is the posterior probability density function (PDF), which defines the Bayesian update of the prior information about the parameter represented by $\pi_{prior}(\boldsymbol{\theta}_i|M_i, \mathcal{M})$, which generally may not depend on the scenario $\mathcal{S}$. The term $\pi_{like}(\mathbf{D}|\boldsymbol{\theta}, M_i, \mathcal{M}, \mathcal{S})$ is the likelihood PDF, and $\pi_{evid}(\mathbf{D}|M_i, \mathcal{M}, \mathcal{S})$ is the evidence, which is the probability of observed data,

$$\pi_{evid}(\mathbf{D}|M_i, \mathcal{M}, \mathcal{S}) = \int_{\Theta_i} \pi_{like}(\mathbf{D}|\boldsymbol{\theta}_i, M_i, \mathcal{M}, \mathcal{S})\, \pi_{prior}(\boldsymbol{\theta}_i|M_i, \mathcal{M})\, d\boldsymbol{\theta}. \tag{27}$$

A useful point estimate is the maximum a posteriori (MAP) of the parameters,

$$\boldsymbol{\theta}_i^{\text{MAP}} = \underset{\theta}{\text{argmax}}\, \pi_{post}(\boldsymbol{\theta}_i|\mathbf{D}, M_i, \mathcal{M}, \mathcal{S}). \tag{28}$$

The statistical discrepancy between the observational data $\mathbf{D}$ and corresponding model output $\mathcal{Y}_{M_i,\mathcal{S}}$, known as the *noise model*, determines the form of the likelihood PDF in (26). To infer parameters of the strain gradient plasticity models from stress–strain data generated by the DDD simulations, we use the log-likelihood function,

$$\ln(\pi_{\text{like}}(\mathbf{D}|\boldsymbol{\theta}_i, M_i, \mathcal{M}, \mathcal{S}) = -\frac{1}{2}\ln(2\pi) - \ln(\sigma_{\text{noise}}) - \frac{1}{2}\frac{\sum_{j=1}^{N_D}(T^j_{M_i,\mathcal{S}} - T^j_{\mathbf{D},\mathcal{S}})^2}{\sigma^2_{\text{noise}}}, \tag{29}$$

where N_D is the number of independent and identically distributed (i.i.d.) data points and $T^j_{\mathbf{D}}$ and $T^j_{Y_{M_i}}$ are the uniaxial stress values obtained from the DDD and the strain gradient model, respectively. The likelihood (29) is derived based on a Gaussian noise model in which data noise and modeling error are additive [69] to make up the total error $\boldsymbol{\epsilon} \sim \mathcal{N}(\mathbf{0}, \sigma^2_{\text{noise}}\mathbf{I})$ with σ^2_{noise} being the noise variance. A careful characterization of the noise variance is crucial to accurate Bayesian inference. Underestimating the noise levels will lead to overfitting the model to measurement and modeling errors, leading to overconfident and biased parameter estimation, while overestimated σ^2_{noise} may lead to disregarding information encoded in the data. We further assume that the modeling errors are proportional to measurements noise, such that

$$\sigma^2_{\text{noise}}\mathbf{I} = m(\sigma^j_D)^2\mathbf{I}, \quad j = 1, 2, \ldots, N_D \tag{30}$$

where σ^j_D is the variance of each data point, $\mathbf{I}$ is an $N_D \times N_D$ identity matrix, and m is called the noise multiplier. To balance the trade-off between the prior of the model parameters and data misfit in the likelihood, we view m as a hyper-parameter to be calculated in the Bayesian inference process. Since the likelihood (29) belongs to the inverse-gamma family, we chose the prior of the noise multiplier to be an inverse gamma function with the mean of 1.0 and the standard deviation of 0.1 [70]. Finally, the numerical solution of Bayesian inference (26) in this work relies on the Delayed Rejection Adaptive Metropolis (DRAM) algorithm [71] as implemented in the open-source library DAKOTA [72].

3.1.3. Model plausibility

Rearranging Bayes' Rule (26), the evidence $\pi_{evid}(\mathbf{D}|M_i, \mathcal{M}, \mathcal{S})$ is realized as a trade-off between how well the model M_i fits the data and the amount of information we gain about the model parameters $\boldsymbol{\theta}_i$ from data [73]. Thus, the model evidence can be viewed as a new likelihood function of the Bayes' Theorem over the models in the set $\mathcal{M}$ [1]. The corresponding posterior, for each model,

$$\rho_i = \pi_{post}(M_i|\mathbf{D}, \mathcal{M}, \mathcal{S}) = \frac{\pi_{evid}(\mathbf{D}|M_i, \mathcal{M}, \mathcal{S})\pi_{prior}(M_i|\mathcal{M})}{\sum_{i=1}^{m}\pi_{evid}(\mathbf{D}|M_i, \mathcal{M}, \mathcal{S})\pi_{prior}(M_i|\mathcal{M})}, \quad i = 1, 2, \ldots, P. \tag{31}$$

is called the posterior model plausibility. The prior model plausibility $\pi_{prior}(M_i|\mathcal{M})$ captures the modeler's belief in the predictive ability of the model M_i before calibration begins. The denominator of (31) normalizes the set of discrete probability component, such that $\sum_{i=1}^{P}\rho_i = 1$. The model with the largest posterior plausibility is

deemed the most plausible model in the set $\mathcal{M}$. Computing the model evidences and, subsequently, the posterior plausibilities requires evaluation of possibly high-dimension integral in (27). Following [74], we approximate the evidence of M_i at the parameters MAP (28),

$$\pi_{evid}(\mathbf{D}|M_i, \mathcal{M}, \mathcal{S}) = \frac{\pi_{like}(\mathbf{D}|\boldsymbol{\theta}_i^{\text{MAP}}, M_i, \mathcal{M}, \mathcal{S})\pi_{prior}(\boldsymbol{\theta}_i^{\text{MAP}}|M_i, \mathcal{M})}{\pi_{post}(\boldsymbol{\theta}_i^{\text{MAP}}|\mathbf{D}, M_i, \mathcal{M}, \mathcal{S})}. \tag{32}$$

3.2. Calibration, validation, and prediction scenarios

A fundamental aspect of predictive physics-based modeling is the hierarchy of scenarios, each with different observational data, to inform the model parameters. The calibration, validation, and prediction scenarios and the sequence in which the model access to data is conceptualized as levels in a "prediction pyramid", e.g., [2,3,5,75,76]. The calibration scenario $\mathcal{S}_c$ resides at the base of the pyramid representing simple component tests designed to generate calibration data $\mathbf{D}_c$ to inform the model parameters. Traveling upwards, the validation scenario $\mathcal{S}_v$ corresponds to a more complex subsystem to test the accuracy of model prediction against validation data $\mathbf{D}_v$. Several validation scenarios may be taken into account to study the validity of various features of the model. The prediction scenario $\mathcal{S}_p$ is at the peak of the pyramid in which a validated model is used to predict quantities of interest (QoI), usually in the absence of observational data. As we move up the pyramid, the computational cost of the model solution usually increases while the amount of available data decreases.

The choice of the validation scenario is particularly crucial in predictive modeling, owing to the reliance of the unobservable QoIs prediction on the extrapolation of the validation data by the model. The role of the calibration data is to provide a meaningful prior distribution to infer the model parameters from the validation data. Consequently, the prediction capacity of the model is determined by how well the validation data portray features of the QoIs in the prediction scenario. Additionally, for rigorous assessment of model validity, $\mathbf{D}_v$ should deliver adequate information over the $\mathbf{D}_c$, and thus validation scenario cannot convey a simple perturbation of the calibration experiment. As described in the following section, we use these attributes of $\mathbf{D}_v$ to design effective validation scenarios.

3.3. The modified OPAL

Building on the Occam Plausibility Algorithm (OPAL) [8], we propose a systematic strategy to adaptively select the "optimal predictive model" among a set of possible models of a physical event. Here, the "optimal model" is referred to as balancing the trade-off between the model complexity and validity, and the "predictive" ability of the model is secured by the design of *model-specific validation experiments* that, in some sense, reflects the structure of the prediction target (QoI). The modified OPAL is shown in Fig. 3 and involves the following steps:

1. **Initialization.** Construct a set $\mathcal{M}$ of models in (24).
2. **Global Sensitivity Analysis.** Compute parameter sensitivities of each model $M_i(\boldsymbol{\theta}_i)$ in the calibration scenario $\mathcal{S}_c$, with the model output $\mathcal{Y}_{M_i,\mathcal{S}_c}$ set to the calibration observables corresponding to $\mathbf{D}_c$. Based on an acceptable tolerance on the sensitivity indices, the insensitive parameters can be assumed as fixed or deterministic, reducing the space of uncertain parameters in all models.
3. **Occam Categories.** Partition the models in $\mathcal{M}$ based on their complexity (e.g., number of uncertain parameters) into *Occam categories*, with the simplest models designated Category 1, and the most complex model resides in the last category. We, therefore, produce a collection of subsets,

$$\mathcal{M}^l = \left\{M_1^l(\boldsymbol{\theta}_1^l), M_2^l(\boldsymbol{\theta}_2^l), \ldots, M_{L_l}^l(\boldsymbol{\theta}_{L_l}^l)\right\}, \quad l = 1, 2\cdots, H, \tag{33}$$

   where l is the category and $L_l < P$.
4. **Occam Step and Calibration.** Starting with $l = 1$, calibrate all the models in the subset $\mathcal{M}^l$, using Bayesian inference (26) for the calibration scenario $\mathcal{S}_c$,

$$\pi_{post}(\boldsymbol{\theta}_i^l|\mathbf{D}_c, M_i^l, \mathcal{M}^l, \mathcal{S}_c) = \frac{\pi_{like}(\mathbf{D}_c|\boldsymbol{\theta}_i^l, M_i^l, \mathcal{M}^l, \mathcal{S}_c)\pi_{prior}(\boldsymbol{\theta}_i^l|M_i^l, \mathcal{M}^l)}{\pi_{evid}(\mathbf{D}_c|M_i^l, \mathcal{M}^l, \mathcal{S}_c)}, \quad i = 1, 2, \ldots, L_l. \tag{34}$$

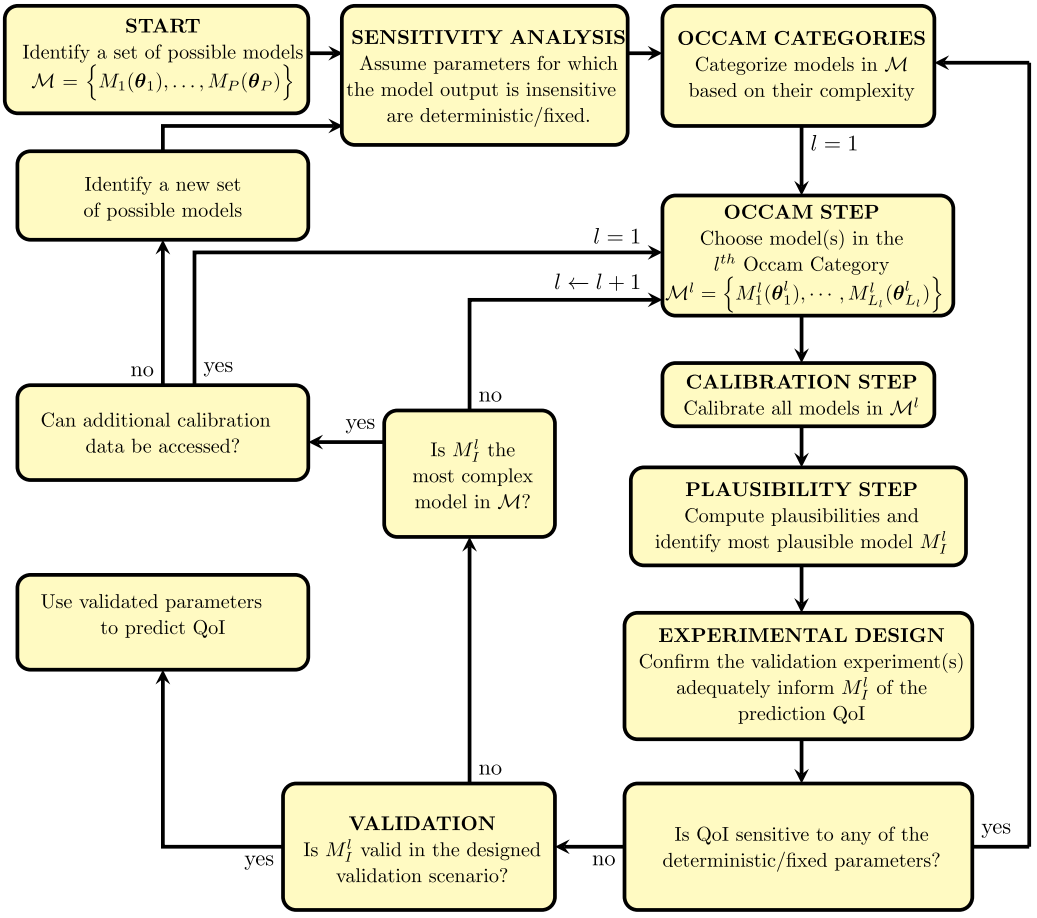

Fig. 3. The modified Occam Plausibility Algorithm: Starting with a set of models, one reduces the uncertain parameter space in each model by fixing the insensitive parameters. The models are then partitioned into categories based on model complexity measures. Beginning with the first category $l = 1$, which consists of the simplest models, Bayesian calibration is done in $\mathcal{S}_c$, and model plausibilities are computed. Finally, model validation is performed on the most plausible model in this category using the designed $\mathcal{S}_v$ for this model, which ensures the validation data adequately informs the model of the target prediction. The model that passes the validation test is deemed the "optimal" predictive model and is used to predict QoI in the prediction scenario $\mathcal{S}_p$.

5. **Plausibility Calculation.** Calculate Bayesian posterior plausibilities $\rho_i^l,\ i = 1, 2, \ldots, L_l$ of the models in Category l. The most plausible model(s) in this category, denoted as $M_I^l(\boldsymbol{\theta}_I^l)$, is then identified.
6. **Experimental Design.** Before subjecting the most plausible model $M_I^l(\boldsymbol{\theta}_I^l)$ in the lth Occam category to a validation test, identify proper validation scenario(s) for this model. We consider two criteria in the experimental design process:
(i) *The validation data* $\mathbf{D}_v$ *must inform the model parameters essential for the prediction QoI, while the associated validation experiment is affordable to conduct.* We propose a method to fulfill this requirement by computing the global sensitivity of the model parameters $\boldsymbol{\theta}_I^l$ in the prediction scenario and for the model output $\mathcal{Y}_{M_I^l,\mathcal{S}_p}$ set equal to the QoI. The sensitivity of the parameters for a proposed validation scenario is also evaluated with model output $\mathcal{Y}_{M_I^l,\mathcal{S}_v}$ equal to the validation observables corresponding to the validation data $\mathbf{D}_v$. These sensitivity analyses can be performed using the initial uncertainty range or calibration posteriors of the model parameters. Suppose the validation sensitivities are in good agreement with those for the

prediction scenario. In that case, the validation experiment is deemed effective and can sufficiently inform the model parameters for predicting the QoI. Using the Sobol indices (25), the criterion for a compelling $\mathcal{S}_v$ is represented as

$$S_{k|M_I^l,\mathcal{S}_p} - (S_{k|M_I^l,\mathcal{S}_v} \pm TOL_s) \geq 0, \quad k = 1, 2 \cdots, K_I^l \tag{35}$$

where K_I^l is the number of model parameters in the vector $\boldsymbol{\theta}_I^l$. If the current validation scenario is ineffective, another $\mathcal{S}_v$ should be proposed based on the experimental feasibility and tested according to (35). We recognize that maximizing the predictive capacity of a model requires model-specific validation experiments, which may not be effective for other models.

(ii) *The validation experiments must reasonably inform the model over the calibration experiments.* Here we use a criterion to ensure that the validation data delivers an acceptable information gain over the calibration experiments, based on the Kullback–Leibler divergence ($D_{KL}(\pi_1 \parallel \pi_2) = \int \pi_1 \ln(\pi_1/\pi_2) d\mathbf{x}$) as a distance measure between the calibration posterior (34) and validation posterior in (37),

$$D_{KL}\left(\pi_{post}(\boldsymbol{\theta}_I^l|\mathbf{D}_v, \mathbf{D}_c, M_I^l, \mathcal{M}^l, \mathcal{S}_c, \mathcal{S}_v)||\pi_{post}(\boldsymbol{\theta}_I^l|\mathbf{D}_c, M_I^l, \mathcal{M}^l, \mathcal{S}_c)\right) \geq TOL_e. \tag{36}$$

Meeting both criteria (35) and (36) ensures that the model-specific validation experiment delivers adequate information over the calibration data while it encodes the structure of the (unobservable) QoI in the prediction scenario.

We remark that the sensitivity analysis results of $M_I^l(\boldsymbol{\theta}_I^l)$ with $\mathcal{Y}_{M_I^l,\mathcal{S}_p}$ being the prediction QoI may reveal that the model(s) need to be recategorized (Step 3). This would necessitate repeating the calibration and plausibility steps.

7. **Validation Step.** With the most plausible model $M_I^l(\boldsymbol{\theta}_I^l)$ and the effective validation scenario $\mathcal{S}_v$ identified, the parameters are again updated via Bayes' rule, using validation data,

$$\pi_{post}(\boldsymbol{\theta}_I^l|\mathbf{D}_v, \mathbf{D}_c, M_I^l, \mathcal{M}^l, \mathcal{S}_c, \mathcal{S}_v) = \frac{\pi_{like}(\mathbf{D}_v|\boldsymbol{\theta}_I^l, \mathbf{D}_c, M_I^l, \mathcal{M}^l, \mathcal{S}_c, \mathcal{S}_v)\pi_{post}(\boldsymbol{\theta}_I^l|\mathbf{D}_c, M_I^l, \mathcal{M}^l, \mathcal{S}_c)}{\pi_{evid}(\mathbf{D}_v|\mathbf{D}_c, M_I^l, \mathcal{M}^l, \mathcal{S}_v)}. \tag{37}$$

We emphasize that the designed validation experiments in the preceding step ensure that the accuracy with which the model agrees with validation observational data $\mathbf{D}_v$ corresponds to the accuracy with which the QoI is predicted in $\mathcal{S}_p$. Thus, to deem the model valid, a distance measure between the model output and data is compared to a given accuracy tolerance TOL_v,

$$D_{KL}\left(\pi(\mathbf{D}_v) \parallel \pi(\boldsymbol{\mathcal{Y}}_{M_I^l,\mathcal{S}_v})\right) \leq TOL_v, \tag{38}$$

where $\pi(\mathbf{D}_v)$ is the PDF of the validation observational data and $\pi(\boldsymbol{\mathcal{Y}}_{M_I^l,\mathcal{S}_v})$ is the model-generated density obtained using the validation-updated parameters.

8. **Iteration and possible refinements.** If the model M_I^l passes the validation test (38), it is the *optimal predictive model* and one can employ it with validated parameters $\pi_{post}(\boldsymbol{\theta}_I^l|\mathbf{D}_v, \mathbf{D}_c, M_I^l, \mathcal{M}^l, \mathcal{S}_c, \mathcal{S}_v)$ to predict the QoI in the prediction scenario $\mathcal{S}_p$. Otherwise, we move on to the next Occam category and repeat Steps 4 through 7 until a valid model is determined. If no models in $\mathcal{M}$ are valid, the model set must be enlarged or additional calibration data acquired.

Concerning the modified OPAL, several remarks are in order:

Remark 1. The presented strategy assumes that while performing global sensitivity analyses have a lower computational cost than the Bayesian inference, calculating parameter sensitivities in the validation and prediction scenarios is computationally intensive and hopelessly impossible for all the models in $\mathcal{M}$. To mitigate the associated computational costs, the global sensitivity analysis is suggested to be performed initially in the $\mathcal{S}_c$ for all models (Step 2). Subsequently, in the design of the validation experiment (Step 6), sensitivity analyses in $\mathcal{S}_v$ and $\mathcal{S}_p$ are performed on the most plausible model in each category. In applications in which conducting parameter sensitivity of the models is feasible in the prediction scenario, the experimental design step can be performed prior to categorizing the models.

Remark 2. The model plausibilities in Step 5 are computed using calibration data, presuming that the calculation of plausibilities in the validation scenario and for a large number of models is rarely feasible due to computational cost. In some cases, however, it is conceivable that validation data could be used for selecting the optimal model.

Remark 3. Although the modified OPAL provides an adaptive strategy for selecting an optimal predictive model, its implementation relies on several (subjective) decisions that the modeler must make for a specific problem. These include the tolerance TOL_s to judge which parameters are essential to be included in the Bayesian calibration (Step 2), acceptable agreement with parameter sensitivity in the prediction scenario to deem a validation experiment as effective (Step 6), and, most importantly, the tolerance TOL_v to judge the model validity (Step 7). Additionally, there are several measures of model complexity, in the sense of Occam's razor, to delineate Occam categories. We have chosen to use the number of uncertain parameters recommended by the sensitivity analysis in Step 2. In general, the decision on the model complexities depends on many other factors and the available resources and ultimately is subjective to the modeler.

4. Numerical results

This section demonstrates the implementation of the modified OPAL to select the optimal predictive continuum plasticity model (Section 2.2) given the observational data furnished by the DDD simulations (Section 2.1) to predict the response of a more complex material system in the absence of observational data.

4.1. Model classes, scenarios, and observables

Different model classes in the set $\mathcal{M}$ derived from the full strain-gradient plasticity, (8) and (19), including various combinations of the energetic and dissipative micro-stresses, and are shown in Table 1. Fig. 4 shows the calibration, validation, and prediction scenarios taken into account in this study for developing predictive discrete-to-continuum multiscale models.

The prediction scenario $\mathcal{S}_p$ is a microelectromechanical (MEMS) capacitive pressure sensor schematically represented at the top of Fig. 4. This microscale device creates a capacitor in which the deformation of the thin film changes the capacitance and provides measurements of the applied load to the sensor. Here, we consider the metallic part of the sensor to be polycrystalline with an average grain size of 450 nm. The target prediction (QoI) is taken as the vertical displacement of the film's midpoint under the applied traction. We note that the DDD model described in Section 2.1 can only simulate idealized geometries and grain morphologies; thus, observational data from high-fidelity simulations is not available in the prediction scenario.

The calibration scenario $\mathcal{S}_c$ is the 9-grain domain under uniaxial tension, and the calibration data $\mathbf{D}_c$ is the DDD stress–strain results (see Fig. 1) for different grain sizes $D = 250$ nm, 500 nm, 1000 nm, and 1500 nm and the film thicknesses of $H = 250$ nm, 500 nm. The validation data $\mathbf{D}_v$ is furnished by the DDD simulations of a more complex subsystem (with the higher cost of acquiring data) consisting of the film thicknesses of $H = 1000$ nm, 1500 nm, and grain sizes $D = 250$ nm, 1000 nm. We note that the 2D continuum plasticity model does not capture the effect of the film thicknesses on the stress–strain model output; thus, different thicknesses in the 3D DDD simulations are viewed as data uncertainty in the Bayesian inference to account for such modeling error.

We take strain energy as the observable that represents size-dependent stress–strain responses in data and model. The sum of the strain energies computed by the strain gradient plasticity model M_i and over the grain sizes in the calibration ($\mathcal{S} = \mathcal{S}_c$) and validation ($\mathcal{S} = \mathcal{S}_v$) scenarios is,

$$\mathcal{Y}_{M_i,\mathcal{S}} = \int_0^{e_f} |T_{M_i,\mathcal{S}}|\, de. \tag{39}$$

Similarly, the strain energy obtained from DDD simulations in each scenario, summed over the corresponding grain sizes and thicknesses, is

$$d_{\mathbf{D},\mathcal{S}} = \int_0^{e_f} |T_{\mathbf{D},\mathcal{S}}|\, de. \tag{40}$$

In (39) and (40), T denotes the uniaxial stress, e is the uniaxial strain, and e_f is the amount of the applied tensile strain in each scenario.

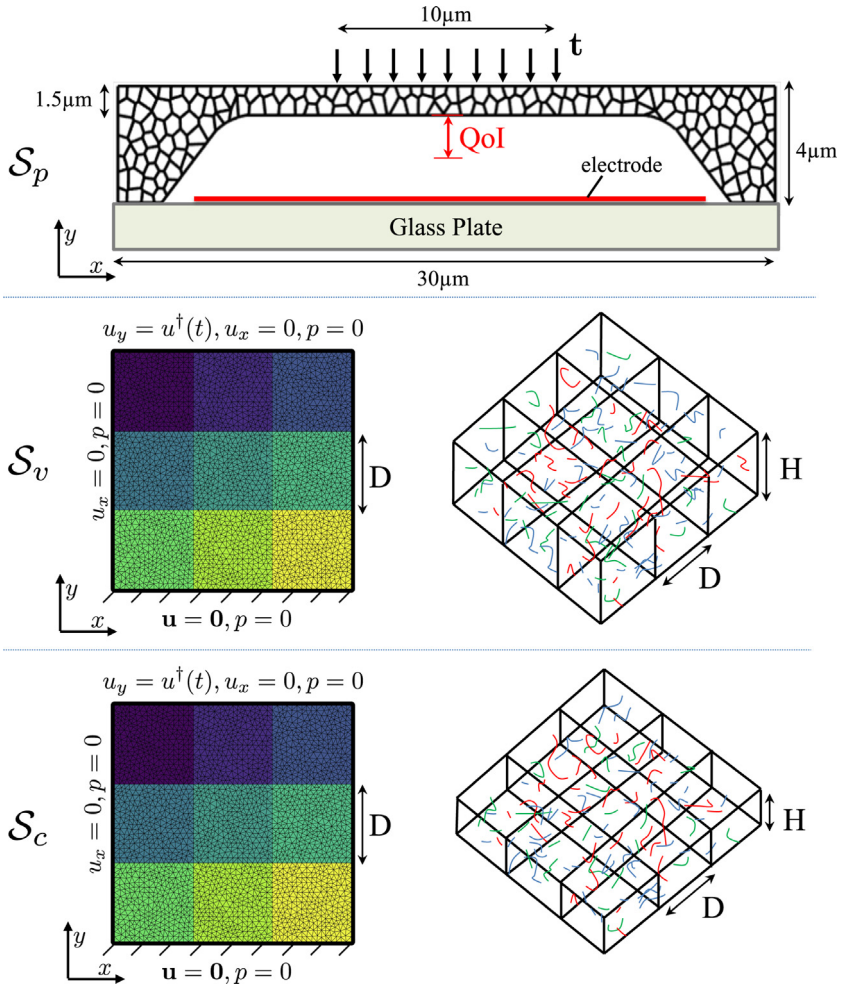

Fig. 4. Illustrations of scenarios considered in the predictive multiscale model of polycrystalline materials: The bottom row shows the calibration scenario $\mathcal{S}_c$, consisting of 9-grain domains in the 3D discrete dislocation simulation with the grain sizes $D = 250$, 500, 1000, and 1500 nm and film thicknesses $H = 250$ nm, 500 nm (right) and the 2D continuum strain gradient plasticity model with similar grain sizes D. The middle row shows the domain of the validation scenario $\mathcal{S}_v$ with $H = 1000$ nm, 1500 nm and $D = 250$ nm, 1000 nm used in DDD simulations (right) and the corresponding continuum model (left). The prediction scenario $\mathcal{S}_p$ at the top is a MEMS pressure sensor with an average grain size of 450 nm, and the unobservable target prediction (QoI) is the vertical displacement of the film under the applied traction $\mathbf{t}$.

4.2. Selection of predictive continuum model via modified OPAL

4.2.1. Sensitivity analysis and Occam categories

Here we perform the sensitivity analysis (Step 2) on the full strain gradient plasticity model M_7 in Table 1, since M_1 to M_6 are sub-models sharing the same parameters. Table 2 shows the model parameters and their initial range of uncertainty used for the sensitivity analysis. Due lack of initial knowledge about the continuum plasticity model parameters, i.e., complete ignorance, uniform distribution is assumed for all the parameters.

Fig. 5(a) presents the results of total sensitivity indices of the parameters $S_{k|M_7,\mathcal{S}_c}$ using the MC estimator described in Section 3.1.1. The model output $\mathcal{Y}_{M_7,\mathcal{S}_c}$ is set to the strain energy measure (39), which reflects the observable stress–strain responses in the calibration scenario. The convergence studies in Fig. 5(b) are the results of five realizations for different numbers of Latin Hypercube samples (LHS) and show that $N_{MC} = 3000$ samples provide sufficient accuracy for estimating the sensitivity indices. Viewing the important parameters to be those with

Table 2
Model parameters of the strain gradient plasticity models and their probability distributions considered for the sensitivity analysis and priors of the Bayesian model calibration.

Parameter	Physical meaning	Probability distributions
ℓ_{dis}	Dissipative length scale	$\mathcal{U}(100, 600)$ nm
ℓ_{en}	Energetic length scale	$\mathcal{U}(0.00, 300)$ nm
Y	Yield strength	$\mathcal{U}(70, 250)$ MPa
h	Isotropic hardening parameter	$\mathcal{U}(0.75, 1 \times 10^{-5})$ GPa
r	Isotropic hardening exponent	$\mathcal{U}(0.2, 450)$
E	Elastic modulus	$\mathcal{U}(145, 170)$ GPa
ν	Poisson's ratio	$\mathcal{U}(0.29, 0.39)$

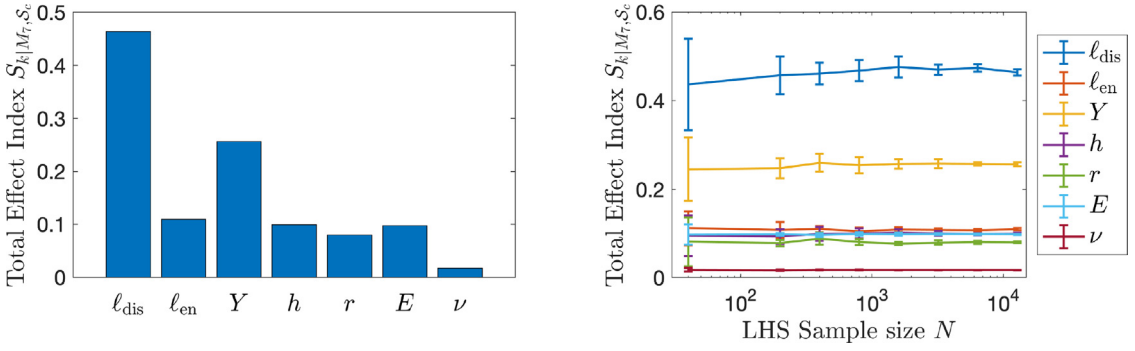

Fig. 5. Variance-based global sensitivity analysis of the full gradient plasticity model for the model output $\mathcal{Y}_{M_7,\mathcal{S}_c}$ being the strain energy measure in (39): (a) The total effect sensitivity indices $S_{k|M_7,\mathcal{S}_c}$; (b) Convergence study of the MC estimator for five realizations and the different number of Latin Hypercube samples.

Table 3
Occam categories of the possible strain gradient plasticity models (Table 1). The model complexity measure is taken as the number of uncertain parameters, and M_7 is the full plasticity model described in Section 2.2. The plausibility and log-evidence values of each model refer, respectively, to ρ_i and $\pi_{evid}(\mathbf{D}_c|M_i, \mathcal{M}^l, \mathcal{S}_c)$, computed in Step 5 of the modified OPAL. The validation metric denotes the distance between the strain energy observables obtained from the validation data and the most plausible model in each category $D_{KL}\left(\pi(d_{\mathbf{D},\mathcal{S}_v}) \parallel \pi(\mathcal{Y}_{M_i,\mathcal{S}_v})\right)$ in Step 7 of the modified OPAL to judge the validity of the model according to (38).

Occam categories	Models	Parameters	Plausibility	Log-evidence	Validation metric
$l = 1$	M_1	E, Y, ℓ_{en}	≈0.02%	−183.7	–
	M_2	E, Y, ℓ_{dis}	≈99.98%	−175.0	0.1304
$l = 2$	M_3	E, Y, h, r	≈0.00%	−211.7	–
	M_4	$E, Y, \ell_{\text{en}}, \ell_{\text{dis}}$	≈100.00%	−174.4	0.0661
$l = 3$	M_5	$E, Y, \ell_{\text{en}}, h, r$	≈0.02%	−193.8	–
	M_6	$E, Y, \ell_{\text{dis}}, h, r$	≈99.98%	−185.2	0.0759
$l = 4$	M_7	$E, Y, \ell_{\text{en}}, \ell_{\text{dis}}, h, r$	–	−184.6	0.0702

the sensitivity index of $S_k > 0.08$, Poisson's ratio is taken as the insensitive parameter, and it is fixed at $\nu = 0.34$ in all sub-models and during the subsequent calibration, validation, and prediction processes.

Guided by the global sensitivity analysis results, the strain gradient plasticity models (Table 1) are classified into four Occam categories shown in Table 3, taking the number of uncertain parameters as the model complexity measure.

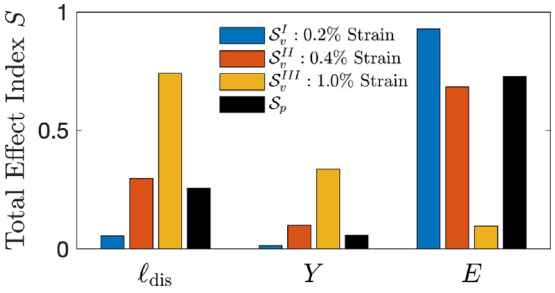

Fig. 6. Design of validation experiment for the model M_2: Total effect sensitivity indices of the model parameters $S_{k|M_2,\mathcal{S}}$, for $k = 1, 2, 3$, are compared in the prediction scenario $\mathcal{S} = \mathcal{S}_p$ for the QoI and the proposed validation scenarios $\mathcal{S} = \mathcal{S}_v^I, \mathcal{S}_v^{II}, \mathcal{S}_v^{III}$ for the strain energy measure (39). Based on the validation experimental design criterion (35), $\mathcal{S}_v^{II}$ is an effective validation experiments that adequately informs M_2 of the prediction QoI.

4.2.2. Occam steps and selecting optimal predictive plasticity model

Next, we evaluate the models in each Occam category following OPAL. The calibration priors of the parameters are presented in Table 2. The Bayesian analyses are conducted using the DRAM algorithm using ten chains with lengths of 2500. Each chain was initialized from different parameter values within the priors' range to explore the parameter space better, and the initial 10% of the chains is considered a burn-in period. We note that the calibration posteriors of the model parameters might have complex features, and approximating these PDFs by known (e.g., Gaussian) distributions to be used as the validation priors may introduce significant errors in the model validation processes. To address this issue, the validation prior is represented by histogram distributions for the solution of the Bayesian validation (37). In this method, the samples of the calibration posterior are treated as a data set, and the distribution of the samples is represented by a number of bins of non-zero width and height, indicating the probability that the uncertain parameter may lie in that bin. Care is given to determine the appropriate number of bins based on the number of available samples to accurately capture features of the parameter distribution.

Occam category 1. Bayesian calibration (34) and computation of the plausibilities of the models in the subset $\mathcal{M}^1 = \{M_1, M_2\}$ in the calibration scenario $\mathcal{S}_c$ indicates M_2 to be the most plausible model in the first category, due to the higher plausibility shown in Table 3. To ensure the validation data adequately informs M_2 of the prediction QoI, we perform the design of the model-specific validation experiment. As the experimental design variable, we consider the total uniaxial strain e_f applied to the domain $\mathcal{S}_v$ in Fig. 4. Accordingly, we propose the following validation scenarios:

- $\mathcal{S}_v^I$: total applied strain $e_f = 0.2\%$
- $\mathcal{S}_v^{II}$: total applied strain $e_f = 0.4\%$
- $\mathcal{S}_v^{III}$: total applied strain $e_f = 1.0\%$

The global sensitivity analyses of model M_2 are performed in the above three scenarios with the model output set to validation observable $\mathcal{Y}_{M_2,\mathcal{S}_v^{(\cdot)}}$ in (39). Additionally, the parameter sensitivities are computed in the prediction scenario $\mathcal{S}_p$ for the model output set equal to the QoI (vertical displacement of the thin film in pressure sensor of Fig. 4). The estimated Sobol indices in the four cases are compared in Fig. 6. Setting the acceptance tolerance in the experimental design objective (35) as $TOL_s = 0.05$, only the sensitivity of parameters in $\mathcal{S}_v^{II}$ is in the range or higher than the ones in $\mathcal{S}_p$. Thus, $\mathcal{S}_v^{II}$ is deemed to be an effective scenario for model validation as the validation data furnished by this scenario $\mathbf{D}_v^{II}$ would adequately inform the important parameters of M_2 for the prediction QoI.

Using the stress–strain data $\mathbf{D}_v^{II}$, generated by the DDD simulations in the identified validation scenario $\mathcal{S}_v^{II}$ for M_2, we update the model parameters $\boldsymbol{\theta}_2 = [E, Y, \ell_{dis}]$ according to (37) to obtain the validation posterior. The kernel density estimation (KDE) of the calibration priors, calibration posteriors, validation posteriors, and the corresponding noise multiplier distributions are shown in Fig. 7. Computing the distance between the calibration and validation posteriors implies that the validation experiment $\mathcal{S}_v^{II}$ reasonably informs the model M_2 over the calibration data,

$$D_{KL}\left(\pi_{post}(\boldsymbol{\theta}_2|\mathbf{D}_v^{II}, \mathbf{D}_c, M_2, \mathcal{M}^1, \mathcal{S}_c, \mathcal{S}_v^{II})||\pi_{post}(\boldsymbol{\theta}_2|\mathbf{D}_c, M_2, \mathcal{M}^1, \mathcal{S}_c)\right) = 110.77 \geq TOL_e = 100. \tag{41}$$

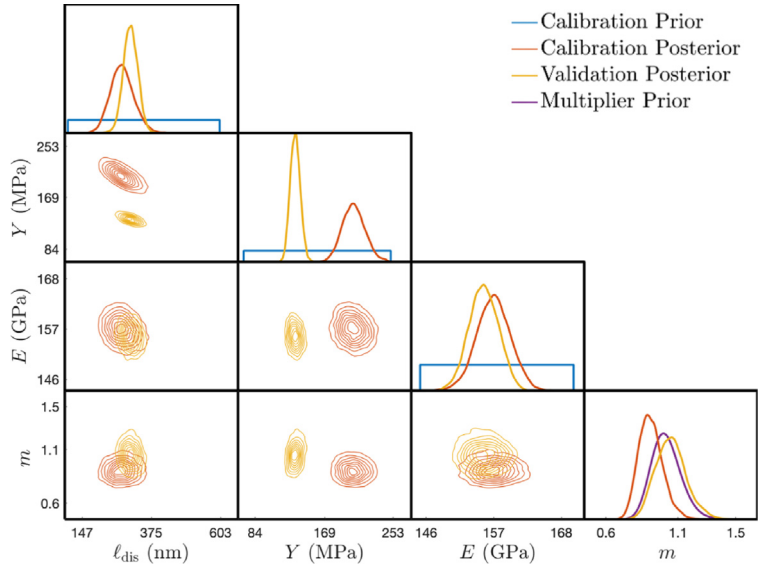

Fig. 7. Bayesian calibration and validation of the model M_2: Marginal distribution of the calibration prior $\pi_{prior}(\boldsymbol{\theta}_2|M_2, \mathcal{M}^1)$ (blue), calibration posterior $\pi_{post}(\boldsymbol{\theta}_2|\mathbf{D}_c, M_2, \mathcal{M}^1, \mathcal{S}_c)$ (red) and validation posterior $\pi_{post}(\boldsymbol{\theta}_2|\mathbf{D}_v^{II}, \mathbf{D}_c, M_2, \mathcal{M}^1, \mathcal{S}_c, \mathcal{S}_v^{II})$ (yellow) probability densities of the parameters and the corresponding noise multiplier m. In both calibration and validation processes, the inverse-Gamma prior (purple) is considered for the hyper-parameter m.

However, subjecting M_2 to the validation test by computing the distance (38) between the average strain energies of the validation data and the one evaluated by the model using the validation posteriors of the parameters in $\mathcal{S}_v^{II}$ (see Table 3) shows that this model is not valid,

$$D_{KL}\left(\pi(d_{\mathbf{D},\mathcal{S}_v^{II}}) \parallel \pi(\mathcal{Y}_{M_2,\mathcal{S}_v^{II}})\right) = 0.1304 \not< TOL_v = 0.1. \tag{42}$$

Occam category 2. We now move to the calibration and plausibility steps of the second category $\mathcal{M}^2 = \{M_3, M_4\}$, that renders M_4 with parameters $\boldsymbol{\theta}_4 = [E, Y, \ell_{\text{en}}, \ell_{\text{dis}}]$ to be the most plausible model. The following validation scenarios are then proposed for this model,

- $\mathcal{S}_v^{II}$: total applied strain $e_f = 0.4\%$
- $\mathcal{S}_v^{IV}$: total applied strain $e_f = 0.5\%$
- $\mathcal{S}_v^{V}$: total applied strain $e_f = 0.7\%$

Comparing the parameter sensitivities in the proposed validation scenarios to $\mathcal{S}_p$ in Fig. 8, indicates that $\mathcal{S}_v^{II}$, the scenario that was effective for M_2, does not adequately inform important parameters (ℓ_{en} and ℓ_{dis}) of M_4 for predicting the QoI. The validation experimental design process of (35), results in selecting $\mathcal{S}_v^{IV}$ as the effective scenario for M_4. The results of Bayesian calibration and validation of the model parameters are presented in Figs. 9 and 10 compares the stress–strain data to the calibrated and validated model outputs. Additionally, the information gain of M_4 from the validation data $\mathbf{D}_v^{IV}$ compared to the calibration data $\mathbf{D}_c$ is within the acceptable range,

$$D_{KL}\left(\pi_{post}(\boldsymbol{\theta}_4|\mathbf{D}_v^{IV}, \mathbf{D}_c, M_4, \mathcal{M}^2, \mathcal{S}_c, \mathcal{S}_v^{IV})||\pi_{post}(\boldsymbol{\theta}_4|\mathbf{D}_c, M_4, \mathcal{M}^2, \mathcal{S}_c)\right) = 190.70 \geq TOL_e = 100. \tag{43}$$

The resulting distributions of the validation observable (strain energy measures in (39) and (40)) shown in Fig. 11 indicate that the validated model M_4 is closer to its designed validation data compared to M_2. Despite the similar model evidences of M_2 and M_4 with respect to the calibration data (see Table 3), the model M_4 with the validation posterior of the parameters $\pi_{post}(\boldsymbol{\theta}_4|\mathbf{D}_v^{IV}, \mathbf{D}_c, M_4, \mathcal{M}^1, \mathcal{S}_c, \mathcal{S}_v^{IV})$ is a valid model as it passes the validation test,

$$D_{KL}\left(\pi(d_{\mathbf{D},\mathcal{S}_v^{IV}}) \parallel \pi(\mathcal{Y}_{M_4,\mathcal{S}_v^{IV}})\right) = 0.0661 \leq TOL_v = 0.1. \tag{44}$$

Thus, according to the definitions in Section 3.3 and given the DDD simulations, the model M_4 is deemed the optimal predictive strain gradient plasticity model among the possible models in Table 1. This suggests that isotropic

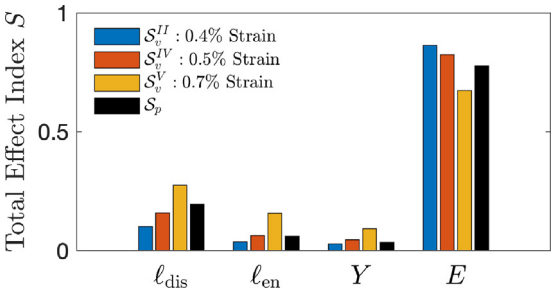

Fig. 8. Design of validation experiment for the model M_4. Total effect sensitivity indices of the model parameters $S_{k|M_4,\mathcal{S}}, k = 1, \ldots, 4$ are compared in the prediction scenario $\mathcal{S} = \mathcal{S}_p$ for the QoI and the proposed validation scenarios $\mathcal{S} = \mathcal{S}_v^{II}, \mathcal{S}_v^{IV}, \mathcal{S}_v^{V}$ for the strain energy measure (39). Based on the validation experimental design criterion (35), $\mathcal{S}_v^{IV}$ is an effective validation experiments that adequately informs M_4 of the prediction QoI.

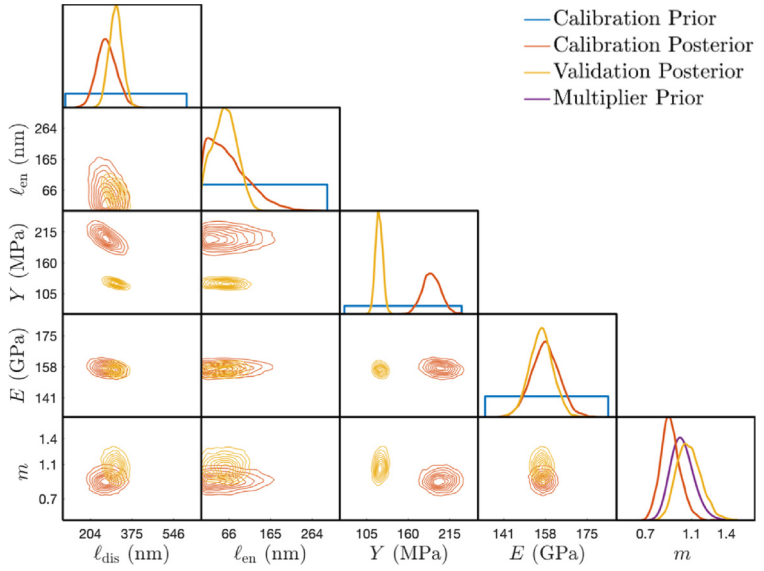

Fig. 9. Bayesian calibration and validation of the model M_4: Marginal distribution of the calibration prior $\pi_{prior}(\boldsymbol{\theta}_4|M_4, \mathcal{M}^2)$ (blue), calibration posterior $\pi_{post}(\boldsymbol{\theta}_4|\mathbf{D}_c, M_4, \mathcal{M}^2, \mathcal{S}_c)$ (red) and validation posterior $\pi_{post}(\boldsymbol{\theta}_4|\mathbf{D}_v^{IV}, \mathbf{D}_c, M_4, \mathcal{M}^2, \mathcal{S}_c, \mathcal{S}_v^{II})$ (yellow) probability densities of the parameters and the corresponding noise multiplier (hyper-parameter) m. In both calibration and validation processes, the inverse-Gamma prior (purple) is considered for the hyper-parameter m.

hardening governed by the microstress $\mathbf{Q}_{\text{en}}$ (with parameters h and r) is not an essential mechanism contributing to the plastic deformation in the current problem and can be eliminated from the full model M_7. To examine the performance of the more complex models M_5, M_6, and M_7, we continue OPAL in categories 3 and 4. The results presented in Table 1 indicate that although both M_6 and M_7 are valid models according to the criterion (38), they do not provide better prediction over the optimal predictive model M_4, as judged by their higher validation metric values. Thus, the predictive abilities of more powerful models that have, for example, more free parameters depend on the priors and how well the observational data inform those parameters.

4.2.3. Impact of noise model on the Bayesian analyses

To achieve unbiased Bayesian calibration and validation while avoiding overfitting the model to measurement and model errors, we introduced the hyper-parameter (noise multiplier) m in (30) for characterizing the noise model. The posteriors of m computed in Bayesian analyses of models M_2 and M_4 are shown in Figs. 7 and 9. In both cases, the calibration posteriors of noise multipliers have a peak of around 0.85, indicating that a smaller total error

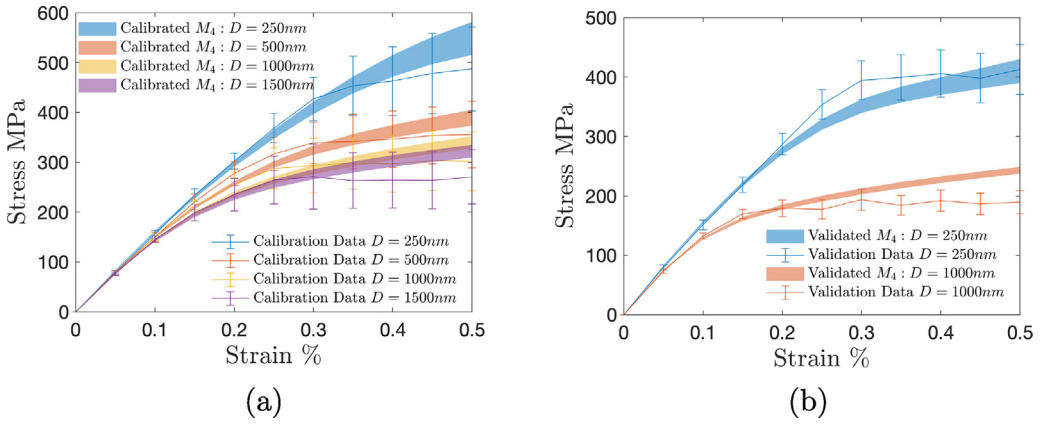

Fig. 10. Comparison of the model M_4 prediction with the stress–strain data furnished by the DDD simulations with different grain sizes: (a) the calibration data $\mathbf{D}_c$ and the model prediction using the calibration posterior of the parameters $\pi_{post}(\boldsymbol{\theta}_4|\mathbf{D}_c, M_4, \mathcal{M}^2, \mathcal{S}_c)$, (b) the model specific validation data $\mathbf{D}_v^{IV}$ and the model prediction using the validation posterior of the parameters $\pi_{post}(\boldsymbol{\theta}_4|\mathbf{D}_v^{IV}, \mathbf{D}_c, M_4, \mathcal{M}^2, \mathcal{S}_c, \mathcal{S}_v^{IV})$. The error bars in observational data indicate uncertainty in 3D DDD simulations due to different initial dislocation configurations and film thicknesses.

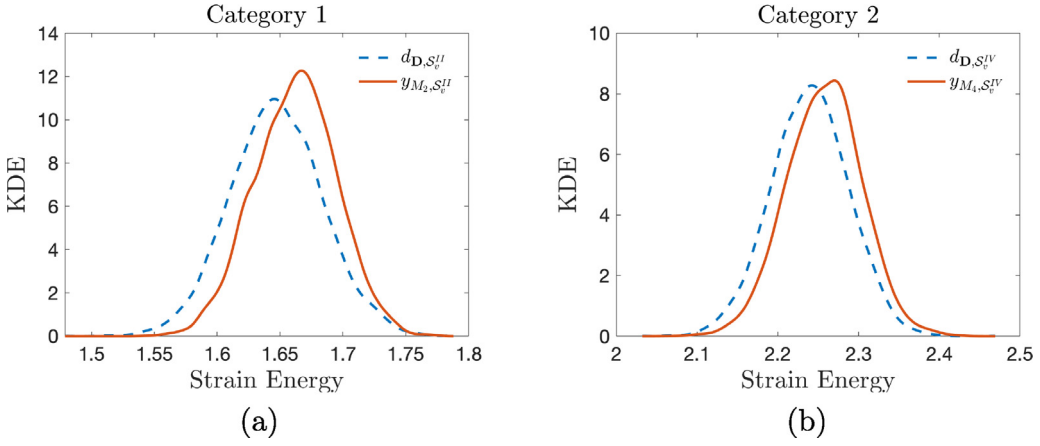

Fig. 11. Distributions of the validation observables ($\mathcal{Y}_{M_i,\mathcal{S}}$ in (39)) yielded by the most plausible model in each category and the corresponding measure ($d_{\mathbf{D},\mathcal{S}}$ in (40)) furnished by DDD simulations in the model specific validation scenarios: (a) Model M_2 using the validation posteriors $\pi_{post}(\boldsymbol{\theta}_2|\mathbf{D}_v^{II}, \mathbf{D}_c, M_2, \mathcal{M}^1, \mathcal{S}_c, \mathcal{S}_v^{II})$ with the corresponding validation data $\mathbf{D}_v^{II}$, (b) Model M_4 using the validation posteriors $\pi_{post}(\boldsymbol{\theta}_4|\mathbf{D}_v^{IV}, \mathbf{D}_c, M_4, \mathcal{M}^2, \mathcal{S}_c, \mathcal{S}_v^{IV})$ with the corresponding validation data $\mathbf{D}_v^{IV}$. The M_4 is deemed valid and thus optimal predictive strain gradient plasticity model.

than the average data variance is needed for robust Bayesian inference. The resulting higher contribution of data misfit to the parameter inference than the priors is due to assigning noninformative (uniform) priors to $\boldsymbol{\theta}_2$ and $\boldsymbol{\theta}_4$ in the Bayesian calibration process. However, due to leveraging calibration posteriors as the prior of the Bayesian validation process (37), the validation posteriors of m nearly have the means of 1.0 and the standard deviations of 0.1, similar to its prior. The noise multiplier close to one implies that, in the validation processes, the average data variance over all the data points is adequate to balance the trade-off between data misfit in the likelihood function and the parameter priors.

4.3. Computational prediction using the optimal model

The optimal predictive strain gradient plasticity model M_4 with the validation posterior of the parameters $\pi_{post}(\boldsymbol{\theta}_4|\mathbf{D}_v^{IV}, \mathbf{D}_c, M_4, \mathcal{M}^2, \mathcal{S}_c, \mathcal{S}_v^{IV})$ obtained from the DDD simulations, is then used to predict the response of

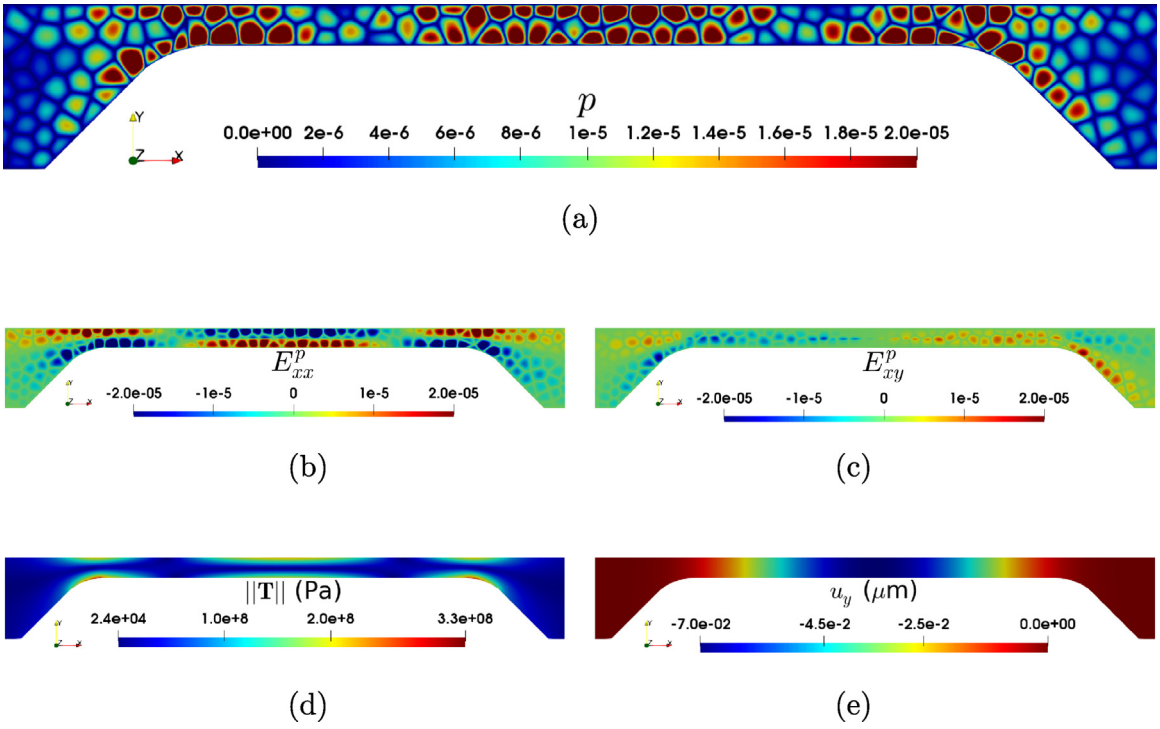

Fig. 12. Computational prediction of the polycrystalline MEMS pressure sensor using the optimal predictive strain gradient plasticity model M_4 and the MAP values of the validation posterior of the model parameters: E = 156.44 GPa, Y = 122.7 MPa, ℓ_{en} = 60.1 nm, ℓ_{dis} = 307.6 nm. (a) equivalent plastic strain $p = \|\mathbf{E}^p\|$, (b, c) components of the plastic strain tensor $\mathbf{E}^p$, along xx and xy, (d) the magnitude of the Cauchy stress tensor $\mathbf{T}$, (e) vertical displacement u_y.

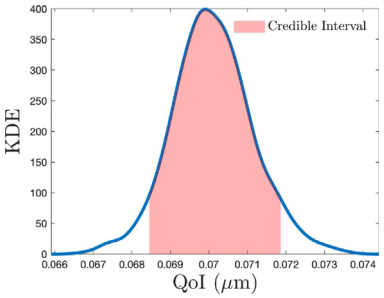

Fig. 13. Computational prediction of the QoI in $\mathcal{S}_p$, using the optimal predictive plasticity model M_4 and validated posteriors of the parameters.

the pressure sensor ($\mathcal{S}_p$ in Fig. 4). The applied traction of $\mathbf{t}$ =(0.0, 2.185) MPa/μm along (x, y) axes is taken into account over the middle 10 μm of the top surface, and zero displacement $\mathbf{u} = \mathbf{0}$ and zero vertical displacement $u_y = 0$ boundary conditions are applied to the bottom and side surfaces, respectively. Additionally, micro-hard boundary conditions with $p = 0$ are imposed on all the external surfaces, describing the pile-up of dislocations achieved by the surface passivation of the MEMS device. Fig. 12 shows stress, displacement, and plastic strain contours computed using the MAP values of the model parameters, estimated from the solution of the validation posterior. The significant accumulated plastic strain in the grains located in the middle of the domain and close to the supports is due to the strain developments during the thin film bending, leading to higher compressive and tensile E^p_{xx} in those regions.

To characterize the reliability of the strain gradient plasticity model in predicting the QoI, we propagate the parametric uncertainty through the model solution in the prediction scenario $\mathcal{S}_p$. Due to the high computational

cost of using all samples for the Bayesian solution obtained via the DRAM algorithm, we leverage a MC method to randomly and uniformly draw sets of samples from the validation posterior distribution of parameters to solve the statistical forward problem. We note that this MC method is valid only if the sampled parameters from the distribution are i.i.d, as the validation posterior of the model parameters here. Using 1000 samples from the parameters validation posterior, model M_4 is solved to obtain the corresponding values of the vertical displacement in the middle of the thin film (QoI). The probability distribution of the QoI, $\pi(Q)$ is shown in Fig. 13, denoting the following mean and 95% credible interval estimations of the computational prediction,

$$\mathbb{E}(Q) = 0.0701 \ \mu\text{m}, \quad \mathcal{CI}(Q) = [0.0685, 0.0719] \ \mu\text{m}. \tag{45}$$

5. Conclusions

This work provides improvement and refinement of steps in the OPAL for selecting an optimal predictive model among a set of possible physics-based models with different fidelities and complexities. The main contribution of this study is to address the non-trivial task of designing model-specific validation experiments to provide validation data that reflect features of the prediction QoI. The application of the modified framework in selecting the strain gradient plasticity models, given the discrete dislocation dynamics data, is provided to predict the response of a polycrystal MEMS pressure sensor beyond observational data. The results indicate that while both energetic and dissipative gradient-dependent micro-stresses are needed to predict the deformation of the microscale material system, eliminating the isotropic hardening term delivers a sufficiently accurate computational prediction of the vertical displacement (QoI). Additionally, the more complex models that have more parameters do not deliver better computational predictions over the optimal model.

We remark that the model selection strategy presented in this work should not be mistaken by the view that"*the complexity of the predictive model should be consistent with the amount of available data*". This idea suggests that when data is insufficient, we should use a simpler model even though that model is known to be incapable of representing the accurate physics of the problem. Attempting to match the models' fidelity to the amount of data is one of the leading causes of overconfident predictions. However, the OPAL framework relies on Bayesian inference in which the model choice is a matter of prior belief on parameters and the model itself and does not depend on the amount of data. Even though acquiring large-scale data from a physical system might be conceivable, data is always incomplete and contaminated with uncertainty. The philosophy in constructing the set of possible models $\mathcal{M}$, suggested by the classical works of Box and Tiao [77] and MacKay [78], is to incorporate (i) the models we genuinely believe in; and (ii) every imaginable sub-models. Moreover, the steps of OPAL can be enriched by the methods to account for unidentifiable and correlated parameters of the models. However, the main goal of the current framework is to ensure sufficient predictive ability of the selected model through testing the model validity given effective validation data. Finally, as indicated in the body of the manuscript, the presented model selection strategy relies on several assumptions applicable to a wide range of modeling problems across science, engineering, and medicine. However, the implementation of OPAL to a specific problem depends on several factors, including the computational feasibility of each step, the measure of model complexity, and validation tolerance that ultimately are *subjective* decisions of the modeler.

In summary, this study shows that the predictive abilities of computational models depend on their parameter priors and how well the observational data inform those parameters. Thus, balancing the model complexity and carefully planned validation data are essential features for reliable computational predictions of complex physical phenomena. The framework demonstrated in this work attempts to address these challenging issues, while possibilities for its enhancement exist and are the subject of future work.

Declaration of competing interest

The authors declare that they have no known competing financial interests or personal relationships that could have appeared to influence the work reported in this paper.

Data availability

Data will be made available on request.

Acknowledgments

DF and JT acknowledge the financial support from the U.S. National Science Foundation (NSF) CAREER Award CMMI-2143662. The authors gratefully acknowledge the helpful discussions with Dr. Richard LeSar, of the Iowa State University, on the discrete dislocation dynamics simulations used in this work. The authors also acknowledge the support provided by the Center for Computational Research at the University at Buffalo. Sandia National Laboratories is a multimission laboratory managed and operated by National Technology & Engineering Solutions of Sandia, LLC, a wholly owned subsidiary of Honeywell International Inc., for the U.S. Department of Energy's National Nuclear Security Administration under contract DE-NA0003525. This paper describes objective technical results and analysis. Any subjective views or opinions that might be expressed in the paper do not necessarily represent the views of the U.S. Department of Energy or the United States Government.

It is with great pleasure that we contribute this study in honor of our dear colleague, mentor, and visionary in the field of computational science and engineering, Professor John Tinsley Oden. We thank him for his numerous contributions to this field, for his statesmanship, and for his leadership over the many years of development of the subject of computational engineering.

References

[1] J.T. Oden, I. Babuška, D. Faghihi, Predictive computational science: Computer predictions in the presence of uncertainty, Encyclopedia of Comput. Mech. Second Edition (2017) 1–26.
[2] T. Oden, R. Moser, O. Ghattas, Computer predictions with quantified uncertainty, part I, SIAM News 43 (9) (2010) 1–3.
[3] J.T. Oden, R. Moser, O. Ghattas, Computer predictions with quantified uncertainty, part II, SIAM News 43 (10) (2010) 1–4.
[4] A.E. Tallman, L.P. Swiler, Y. Wang, D.L. McDowell, 14 - Hierarchical multiscale model calibration and validation for materials applications, in: Y. Wang, D.L. McDowell (Eds.), Uncertainty Quantification in Multiscale Materials Modeling, in: Elsevier Series in Mechanics of Advanced Materials, Woodhead Publishing, 2020, pp. 449–471, http://dx.doi.org/10.1016/B978-0-08-102941-1.00014-6.
[5] I. Babuška, F. Nobile, R. Tempone, A systematic approach to model validation based on Bayesian updates and prediction related rejection criteria, Comput. Methods Appl. Mech. Engrg. 197 (29) (2008) 2517–2539, http://dx.doi.org/10.1016/j.cma.2007.08.031, Validation Challenge Workshop.
[6] C. Truesdell, A. Pipkin, W. Noll, The non-linear field theories of mechanics, The American Society of Mechanical Engineers (ASME), 1965.
[7] M.E. Gurtin, An Introduction To Continuum Mechanics, Academic Press, 1982.
[8] K. Farrell, J.T. Oden, D. Faghihi, A Bayesian framework for adaptive selection, calibration, and validation of coarse-grained models of atomistic systems, J. Comput. Phys. 295 (2015) 189–208.
[9] J.T. Oden, K. Farrell, D. Faghihi, Estimation of error in observables of coarse-grained models of atomic systems, Adv. Model. Simul. Eng. Sci. 2 (1) (2015) 1–20.
[10] E.A. Lima, D. Faghihi, R. Philley, J. Yang, J. Virostko, C.M. Phillips, T.E. Yankeelov, Bayesian calibration of a stochastic, multiscale agent-based model for predicting in vitro tumor growth, PLoS Comput. Biol. 17 (11) (2021) e1008845.
[11] J.T. Oden, E.A. Lima, R.C. Almeida, Y. Feng, M.N. Rylander, D. Fuentes, D. Faghihi, M.M. Rahman, M. DeWitt, M. Gadde, et al., Toward predictive multiscale modeling of vascular tumor growth, Arch. Comput. Methods Eng. 23 (4) (2016) 735–779.
[12] E. Lima, J. Oden, D. Hormuth, T. Yankeelov, R. Almeida, Selection, calibration, and validation of models of tumor growth, Math. Models Methods Appl. Sci. 26 (12) (2016) 2341–2368.
[13] E. Lima, J. Oden, B. Wohlmuth, A. Shahmoradi, D. Hormuth II, T. Yankeelov, L. Scarabosio, T. Horger, Selection and validation of predictive models of radiation effects on tumor growth based on noninvasive imaging data, Comput. Methods Appl. Mech. Engrg. 327 (2017) 277–305.
[14] C. Zhou, R. LeSar, Dislocation dynamics simulations of the Bauschinger effect in metallic thin films, Comput. Mater. Sci. 54 (2012) 350–355.
[15] J. Tan, U. Villa, N. Shamsaei, S. Shao, H.M. Zbib, D. Faghihi, A predictive discrete-continuum multiscale model of plasticity with quantified uncertainty, Int. J. Plast. 138 (2021) 102935.
[16] G.Z. Voyiadjis, D. Faghihi, Y. Zhang, A theory for grain boundaries with strain-gradient plasticity, Int. J. Solids Struct. 51 (10) (2014) 1872–1889.
[17] Z. Wang, N. Ghoniem, S. Swaminarayan, R. LeSar, A parallel algorithm for 3D dislocation dynamics, J. Comput. Phys. 219 (2) (2006) 608–621.
[18] C. Zhou, Dislocation Dynamics Simulations of Plasticity At Small Scales, Iowa State University, 2010.
[19] N. Ghoniem, M., S.-H. Tong, L. Sun, Parametric dislocation dynamics: a thermodynamics-based approach to investigations of mesoscopic plastic deformation, Phys. Rev. B 61 (2) (2000) 913.
[20] C. Zhou, R. LeSar, Dislocation dynamics simulations of plasticity in polycrystalline thin films, Int. J. Plast. 30 (2012) 185–201.
[21] D. Faghihi, Continuum and crystal strain gradient plasticity with energetic and dissipative length scales, Doctoral Dissertation, Louisiana State University, 2012.
[22] D. Faghihi, G.Z. Voyiadjis, Thermal and mechanical responses of BCC metals to the fast-transient process in small volumes, J. Nanomech. Micromech 2 (3) (2012) 29–41.

[23] D. Faghihi, G.Z. Voyiadjis, A thermodynamic consistent model for coupled strain-gradient plasticity with temperature, J. Eng. Mater. Technol 136 (1) (2014).
[24] M.E. Gurtin, L. Anand, A theory of strain-gradient plasticity for isotropic, plastically irrotational materials. Part I: Small deformations, J. Mech. Phys. Solids 53 (7) (2005) 1624–1649.
[25] M.E. Gurtin, B.D. Reddy, Gradient single-crystal plasticity within a Mises–Hill framework based on a new formulation of self-and latent-hardening, J. Mech. Phys. Solids 68 (2014) 134–160.
[26] M.E. Gurtin, N. Ohno, A gradient theory of small-deformation, single-crystal plasticity that accounts for GND-induced interactions between slip systems, J. Mech. Phys. Solids 59 (2) (2011) 320–343.
[27] J. Nye, Some geometrical relations in dislocated crystals, Acta Metall. 1 (2) (1953) 153–162.
[28] G.Z. Voyiadjis, D. Faghihi, The effect of temperature on interfacial gradient plasticity in metallic thin films, J. Surf. Interf. Mater. 1 (1) (2013) 30–42.
[29] M.E. Gurtin, B.D. Reddy, Alternative formulations of isotropic hardening for Mises materials, and associated variational inequalities, Contin. Mech. Thermodyn. 21 (3) (2009) 237–250.
[30] M.E. Gurtin, L. Anand, Thermodynamics applied to gradient theories involving the accumulated plastic strain: the theories of Aifantis and Fleck and Hutchinson and their generalization, J. Mech. Phys. Solids 57 (3) (2009) 405–421.
[31] G.Z. Voyiadjis, D. Faghihi, Thermo-mechanical strain gradient plasticity with energetic and dissipative length scales, Int. J. Plast. 30 (2012) 218–247.
[32] G.Z. Voyiadjis, D. Faghihi, Overview of enhanced continuum theories for thermal and mechanical responses of the microsystems in the fast-transient process, J. Eng. Mater. Technol 136 (4) (2014).
[33] G.Z. Voyiadjis, D. Faghihi, Gradient plasticity for thermo-mechanical processes in metals with length and time scales, Phil. Mag. 93 (9) (2013) 1013–1053.
[34] D. Faghihi, G.Z. Voyiadjis, T. Park, Coupled thermomechanical modeling of small volume fcc metals, J. Eng. Mater. Technol 135 (2) (2013).
[35] P. Gudmundson, C.F. Dahlberg, Isotropic strain gradient plasticity model based on self-energies of dislocations and the Taylor model for plastic dissipation, Int. J. Plast. 121 (2019) 1–20.
[36] N. Fleck, J. Willis, A mathematical basis for strain-gradient plasticity theory – Part I: Scalar plastic multiplier, J. Mech. Phys. Solids 57 (1) (2009) 161–177.
[37] G.Z. Voyiadjis, Y. Song, Strain gradient continuum plasticity theories: theoretical, numerical and experimental investigations, Int. J. Plast. 121 (2019) 21–75.
[38] E.C. Aifantis, On the microstructural origin of certain inelastic models, 1984.
[39] E.C. Aifantis, The physics of plastic deformation, Int. J. Plast. 3 (3) (1987) 211–247.
[40] C.F. Niordson, V. Tvergaard, Instabilities in power law gradient hardening materials, Int. J. Solids Struct. 42 (9–10) (2005) 2559–2573.
[41] N. Fleck, J. Hutchinson, A phenomenological theory for strain gradient effects in plasticity, J. Mech. Phys. Solids 41 (12) (1993) 1825–1857, http://dx.doi.org/10.1016/0022-5096(93)90072-N.
[42] M.E. Gurtin, L. Anand, A theory of strain-gradient plasticity for isotropic, plastically irrotational materials. Part II: Finite deformations, Int. J. Plast. 21 (12) (2005) 2297–2318.
[43] G.Z. Voyiadjis, B. Deliktas, D. Faghihi, A. Lodygowski, Friction coefficient evaluation using physically based viscoplasticity model at the contact region during high velocity sliding, Acta Mech. 213 (1–2) (2010) 39–52.
[44] Y. Song, G.Z. Voyiadjis, Strain gradient finite element model for finite deformation theory: Size effects and shear bands, Comput. Mech. 65 (5) (2020) 1219–1246.
[45] R.K.A. Al-Rub, G.Z. Voyiadjis, D.J. Bammann, A thermodynamic based higher-order gradient theory for size dependent plasticity, Int. J. Solids Struct. 44 (9) (2007) 2888–2923.
[46] R.K. Abu Al-Rub, G.Z. Voyiadjis, E.C. Aifantis, On the thermodynamics of higher-order gradient plasticity for size-effects at the micron and submicron length scales, Int. J. Mater. Product Technol 34 (1–2) (2009) 172–187.
[47] N. Fleck, J. Willis, A mathematical basis for strain-gradient plasticity theory – Part II: Tensorial plastic multiplier, J. Mech. Phys. Solids 57 (7) (2009) 1045–1057.
[48] L. Bardella, Size effects in phenomenological strain gradient plasticity constitutively involving the plastic spin, Internat. J. Engrg. Sci. 48 (5) (2010) 550–568.
[49] P. Fredriksson, P. Gudmundson, Size-dependent yield strength of thin films, Int. J. Plast. 21 (9) (2005) 1834–1854.
[50] G. Voyiadjis, Y. Song, Higher order thermo-mechanical gradient plasticity model: non-proportional loading with energetic and dissipative components, in: Handbook of Nonlocal Continuum Mechanics for Materials and Structures, Springer International Publishing, Cham, Switzerland, 2017.
[51] G.Z. Voyiadjis, Y. Song, T. Park, Higher-order thermomechanical gradient plasticity model with energetic and dissipative components, J. Eng. Mater. Technol 139 (2) (2017).
[52] L. Bardella, C.F. Niordson, Strain gradient plasticity: Theory and implementation, in: Mechanics of Strain Gradient Materials, Springer, 2020, pp. 101–149.
[53] M.E. Gurtin, A gradient theory of small-deformation isotropic plasticity that accounts for the Burgers vector and for dissipation due to plastic spin, J. Mech. Phys. Solids 52 (11) (2004) 2545–2568.
[54] B.D. Reddy, C. Wieners, B. Wohlmuth, Finite element analysis and algorithms for single-crystal strain-gradient plasticity, Internat. J. Numer. Methods Engrg. 90 (6) (2012) 784–804.
[55] B. Reddy, The role of dissipation and defect energy in variational formulations of problems in strain-gradient plasticity. Part 1: polycrystalline plasticity, Contin. Mech. Thermodyn. 23 (6) (2011) 527–549.

[56] C. Carstensen, F. Ebobisse, A. McBride, B. Reddy, P. Steinmann, Some properties of the dissipative model of strain-gradient plasticity, Phil. Mag. 97 (10) (2017) 693–717.
[57] M.S. Alnæs, J. Blechta, J. Hake, A. Johansson, B. Kehlet, A. Logg, C. Richardson, J. Ring, M.E. Rognes, G.N. Wells, The FEniCS project version 1.5, Archive Numer. Softw. 3 (100) (2015) http://dx.doi.org/10.11588/ans.2015.100.20553.
[58] A. Saltelli, I.M. Sobol', About the use of rank transformation in sensitivity analysis of model output, Reliab. Eng. Syst. Saf. 50 (3) (1995) 225–239.
[59] A. Saltelli, P. Annoni, I. Azzini, F. Campolongo, M. Ratto, S. Tarantola, Variance based sensitivity analysis of model output. Design and estimator for the total sensitivity index, Comput. Phys. Comm. 181 (2) (2010) 259–270.
[60] A. Saltelli, M. Ratto, T. Andres, F. Campolongo, J. Cariboni, D. Gatelli, M. Saisana, S. Tarantola, Global sensitivity analysis: The primer, Wiley, 2008.
[61] A. Saltelli, K. Chan, E. Scott, Sensitivity Analysis, in: Wiley paperback series, (2008) Wiley, 2009.
[62] I.M. Sobol', Sensitivity estimates for nonlinear mathematical models, Matematicheskoe Modelirovanie 2 (1990) 112–118.
[63] I.M. Sobol', Sensitivity analysis for non-linear mathematical models, Math. Model. Comput. Exp. 1 (1993) 407–414.
[64] I.M. Sobol', Global sensitivity analysis indices for the investigation of nonlinear mathematical models, Matematicheskoe Modelirovanie 19 (2007) 23–24.
[65] T. Homma, A. Saltelli, Importance measures in global sensitivity analysis of nonlinear models, Reliab. Eng. Syst. Saf. 52 (1) (1996) 1–17.
[66] A. Saltelli, S. Tarantola, On the relative importance of input factors in mathematical models, J. Amer. Statist. Assoc. 97 (459) (2002) 702–709.
[67] A. Saltelli, Making best use of model evaluations to compute sensitivity indices, Comput. Phys. Comm. 145 (2) (2002) 280–297.
[68] E.T. Jaynes, Probability Theory: The Logic of Science, Cambridge University Press, 2003.
[69] M.C. Kennedy, A. O'Hagan, Bayesian calibration of computer models, J. R. Stat. Soc. Ser. B Stat. Methodol. 63 (3) (2001) 425–464.
[70] J. Tan, P. Maleki, L. An, M. Di Luigi, U. Villa, C. Zhou, S. Ren, D. Faghihi, A predictive multiphase model of silica aerogels for building envelope insulations, Comput. Mech. (2022) 1–23.
[71] H. Haario, M. Laine, A. Mira, E. Saksman, DRAM: efficient adaptive MCMC, Stat. Comput. 16 (4) (2006) 339–354.
[72] K. Dalbey, M.S. Eldred, G. Geraci, J.D. Jakeman, K.A. Maupin, J.A. Monschke, D.T. Seidl, L.P. Swiler, A. Tran, F. Menhorn, et al., Dakota, a multilevel parallel object-oriented framework for design optimization parameter estimation uncertainty quantification and sensitivity analysis: Version 6.12 theory manual, Sandia National Lab.(SNL-NM), Albuquerque, NM (United States), 2020.
[73] M. Muto, J.L. Beck, Bayesian updating and model class selection for hysteretic structural models using stochastic simulation, J. Vib. Control 14 (1–2) (2008) 7–34.
[74] L. Wasserman, Bayesian model selection and model averaging, J. Math. Psych. 44 (1) (2000) 92–107.
[75] J.T. Oden, E.E. Prudencio, A. Hawkins-Daarud, Selection and assessment of phenomenological models of tumor growth, Math. Models Methods Appl. Sci. 23 (07) (2013) 1309–1338.
[76] J.T. Oden, E.E. Prudencio, P.T. Bauman, Virtual model validation of complex multiscale systems: Applications to nonlinear elastostatics, Comput. Methods Appl. Mech. Engrg. 266 (2013) 162–184.
[77] G.E. Box, G.C. Tiao, Bayesian Inference in Statistical Analysis, vol. 40, John Wiley & Sons, 1973.
[78] D.J. MacKay, Probable networks and plausible predictions-a review of practical Bayesian methods for supervised neural networks, Network: Comput. Neural Syst. 6 (3) (1995) 469.